Early Permian freshwater silicified stromatolites and oolites from the Krkonoše Piedmont Basin (Bohemian Massif): paleobiology, environmental setting and early diagenesis

Stanislava Vodrážková, Radek Vodrážka, Tomáš Kumpan, Juraj Franců, Markéta Holá & Karel Slavíček

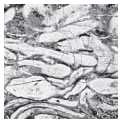

Late Palaeozoic non-marine microbialites remain poorly documented despite their potential significance for understanding terrestrial ecosystems during this period of profound climatic and environmental change. Here we report exceptionally preserved lower Permian (Autunian regional stage ~ Asselian–Sakmarian) silicified stromatolites and oolites from the Krkonoše Piedmont Basin (Bohemian Massif, Czech Republic). Despite their occurrence in Quaternary eluvial and colluvial deposits, multiple lines of evidence suggest formation in a shallow, ephemeral fluvio-lacustrine setting. The stromatolites display a vertical succession of different growth forms, including structures similar to modern sheath-forming cyanobacterial taxa that form fan-like and hemispheroidal colonies with characteristic upright growth, features especially common in modern streams and rivers. Early diagenetic silicification preserved not only delicate stromatolitic architectures but also microbial organic matter. The presence of volcaniclastic material within ooidal cortices and cores, as well as within the rock matrix, indicates contemporaneous volcanic input, which likely provided silica for early replacement of the primary carbonate fabric. This exceptional preservation, facilitated by rapid $CaCO_3$ encrustations of microbial structures and subsequent early silicification, provides rare insights into early Permian terrestrial ecosystems. • Key words: early Permian, Krkonoše Piedmont Basin, stromatolites, oolites, cyanobacteria, silicification.

Vodrážková, S., Vodrážka, R., Kumpan, T., Franců, J., Holá, M. & Slavíček, K. 2025. Early Permian Freshwater Silicified Stromatolites and Oolites from the Krkonoše Piedmont Basin (Bohemian Massif): Paleobiology, Environmental Setting and Early Diagenesis. *Bulletin of Geosciences 100*(*2*), xxx–xxx (12 figures, 2 electronic appendices). Czech Geological Survey, Prague. ISSN 1214-1119. Manuscript received December 10, 2024; accepted in revised form May 21, 2025; published online June 29, 2025; issued Xxxxxx XX, 2025.

Stanislava Vodrážková (corresponding author), Radek Vodrážka & Juraj Franců, Czech Geological Survey, Klárov 3, 118 21 Prague 1, Czech Republic; stanislava.vodrazkova@geology.cz • Tomáš Kumpan & Karel Slavíček, Department of Geological Sciences – Faculty of Science, Masaryk University, Kotlářská 267/2, 611 37 Brno, Czech Republic • Markéta Holá, Department of Chemistry – Faculty of Science, Masaryk University, Kamenice 753/5, 625 00 Brno, Czech Republic

Microbialites, including stromatolites, provide a unique record of geobiological interactions spanning more than 3.4 billion years (Allwood *et al*. 2006, Nutman *et al*. 2016). Modern microbialites inhabit a diverse array of marine and marginal depositional settings, ranging from deep marine environments to coastal ponds (Saint Martin & Saint Martin 2015, Cathalot *et al*. 2021, Reid *et al*. 2024). The variety of terrestrial depositional environments in which modern microbialites occur is even more extensive. These include fluvial systems (*e.g*. Kleinteich *et al*. 2017), cool springs (*e.g*. Rott *et al*. 2012), hot springs (*e.g*. Jones *et al*. 2005), waterfalls and streams (*e.g*. Pentecost 1995, Perri *et al*. 2012), desert ponds (*e.g*. Centeno *et al*. 2012), and even non-aquatic environments, such as caves (*e.g*. Suchý *et al.* 2021) and soils (*e.g*. Robins *et al*. 2015). The geographic distribution of modern microbialites spans a remarkable range of latitudes, from subarctic regions (*e.g*. White *et al*. 2015) to Antarctica (*e.g*. Elster *et al*. 2016), demonstrating their ability to thrive in diverse climatic conditions.

The most common continental depositional setting of modern microbialites (including stromatolites) is lakes (Myshrall *et al*. 2014). These water bodies are characterized by a wide range of physicochemical parameters, including hypersaline conditions (*e.g*. Glunk *et al*. 2011), alkaline environments (*e.g*. Kazmierczak & Kempe 2006), and varying Mg/Ca ratios (*e.g*. Souza-Egipsy *et al*. 2005). In comparison to the widely distributed and common terrestrial microbialites in recent settings, the fossil record of terrestrial microbialites appears to be scarce. This

scarcity can be attributed to preservation bias against terrestrial deposits (Holland 2016, Na *et al*. 2023), overall lower abundance of fossil terrestrial sedimentary deposits compared to marine ones and the general decrease in their quantity with increasing age (Peters & Husson 2017). Therefore, it is not surprising that there is little evidence of lower and middle Paleozoic terrestrial microbialites (*e.g*. Marriott *et al*. 2013, Andrews & Trewin 2014).

During the late Carboniferous–Permian, a profound geodynamic reorganization occurred with the assembly of the supercontinent Pangaea. This was due to the collision of continents of Gondwana and Laurussia and the uplift of the Variscan/Mauretanides/Alleghanian orogens in the equatorial region of Pangaea (*e.g*. Hmich *et al.* 2006). With the formation of the Pangaea supercontinent, the level of continentality has been unprecedented (Lucas *et al*. 2006), and most of the terrestrial Permian is represented by hiatuses or unfossiliferous strata (Rössler 2006). Post-orogenic collapse of the thickened orogenic crust triggered the formation of a series of continental basins in Europe and North Africa (McCann *et al*. 2006, Schneider & Romer 2010), which had a significant effect on the record of terrestrial microbialites during the late Palaeozoic. These newly formed basins created diverse depositional environments where microbial communities could thrive and microbialites were formed. The occurrence of microbialites (including stromatolites and coated grains) has been reported, particularly in lower Permian fluvial, lacustrine, and alluvial fan/playa settings in North Africa, France, Italy, Germany, Poland, and the Czech Republic (Petrascheck 1906; Fediuk 1956; Stapf 1973; Bertrand-Sarfati & Fabre 1974; Schäfer & Stapf 1978; Szulc & Cwizewicz 1989; Freytet *et al*. 1992, 1996, 1999; Gand *et al*. 1993; Kerp *et al*. 1996; Stapf 2005; Rössler *et al*. 2021; Hellwig *et al*. 2023; Trümper *et al*. 2023).

In this study, we document the first occurrence of Autunian (lower Permian) freshwater stromatolites from the Krkonoše Piedmont Basin of the Bohemian Massif, Czech Republic. We aim to focus on (1) characterizing the morphological, compositional, and geochemical features of these stromatolites and oolites, including their biomarkers, trace and rare earth element signatures, (2) determining the timing and mechanisms of their preservation through integrated petrographic and geochemical analysis, and (3) interpreting their depositional conditions.

Geological setting

The Krkonoše Piedmont Basin (KPB) of the Bohemian Massif (Fig. 1) represents an intermontane extensional basin formed during the initial stages of post-orogenic extension following the collapse of the thickened Variscan orogenic crust (McCann *et al*. 2006, Ulrych *et al*. 2006, Schöpfer *et al*. 2022). The upper Carboniferous (Westphalian D) to Triassic (Scythian) infill of the basin consists of deposits of complex fluvial, lacustrine, and alluvial plain systems, predominantly represented by red siliciclastics, coal seams, black shales and carbonate interbeds, as well as products of basic-intermediate and acid volcanism (Blecha *et al.* 1999; Prouza & Tásler 2001; Ulrych *et al*. 2003, 2006; Martínek *et al*. 2006; Opluštil *et al*. 2013, 2016; Stárková & Čáp 2017; Schöpfer *et al.* 2022).

The studied Permian stromatolites, oolites, and oolitic rocks occur predominantly as silicified boulders in Quaternary eluvial and colluvial deposits near the Zlatý Creek in the former settlement Bystřice, NW from Mladé Buky in the KPB (Fig. 2A, GPS: N 50.615277°, E 15.860833°, N 50.619740°, E 15.854050°). A few tens of centimetres thick section of in situ silicified oolitic rocks with permineralized stems and tuffaceous matrix was discovered in an excavated section at the creek bank (GPS: N 50.616666°, E 15.860833°), however, without a record of stromatolites.

According to the Geological Map of the Czech Republic, 1:25 000 (Schovánek *et al.* 2012), Prosečné and Chotěvice formations (in successive order) of Autunian age (~ Asselian–Sakmarian) were mapped here, though no surface outcrops of these formations are exposed in the vicinity of Mladé Buky.

While stromatolites have not been recorded before, Petrascheck (1906) noted the occurrence of silicified oolites from the vicinity of the Mladé Buky and Bystřice (Klinge in German). Similarly, Fediuk (1956) reported siliceous cherts with oolitic texture from this area, attributing their origin to silicification of original limestones based on the presence of $CaCO_3$ remnants within the ooids, which is supported by the field observations of Petrascheck (1906). Rare ooids in KPB were recorded also by Blecha *et al*. (1999) in nearshore carbonates of the Kalná Horizon (Prosečné Formation).

The Prosečné Formation is preserved as an erosional relic in the central and western parts of the KPB, and its substantial part is represented by deposits of temporary lakes and alluvial plains, with documented examples of mudcracks, raindrop imprints, and caliche nodules, indicative of occasional subaerial exposure (Blecha *et al*. 1999). According to Prouza & Tásler (2001), several decimeters to several metres-thick beds of tuffs and tuffites containing euhedral biotite and quartz, referred to as the Horní Branná and Mladé Buky tuffitic horizons, were documented in this unit. These strata are underlain by a few metres-thick succession of andesitic tuffs and tuffites. Importantly, according to these authors, silicite layers were associated with the tuffitic intercalations within the Prosečné Formation.

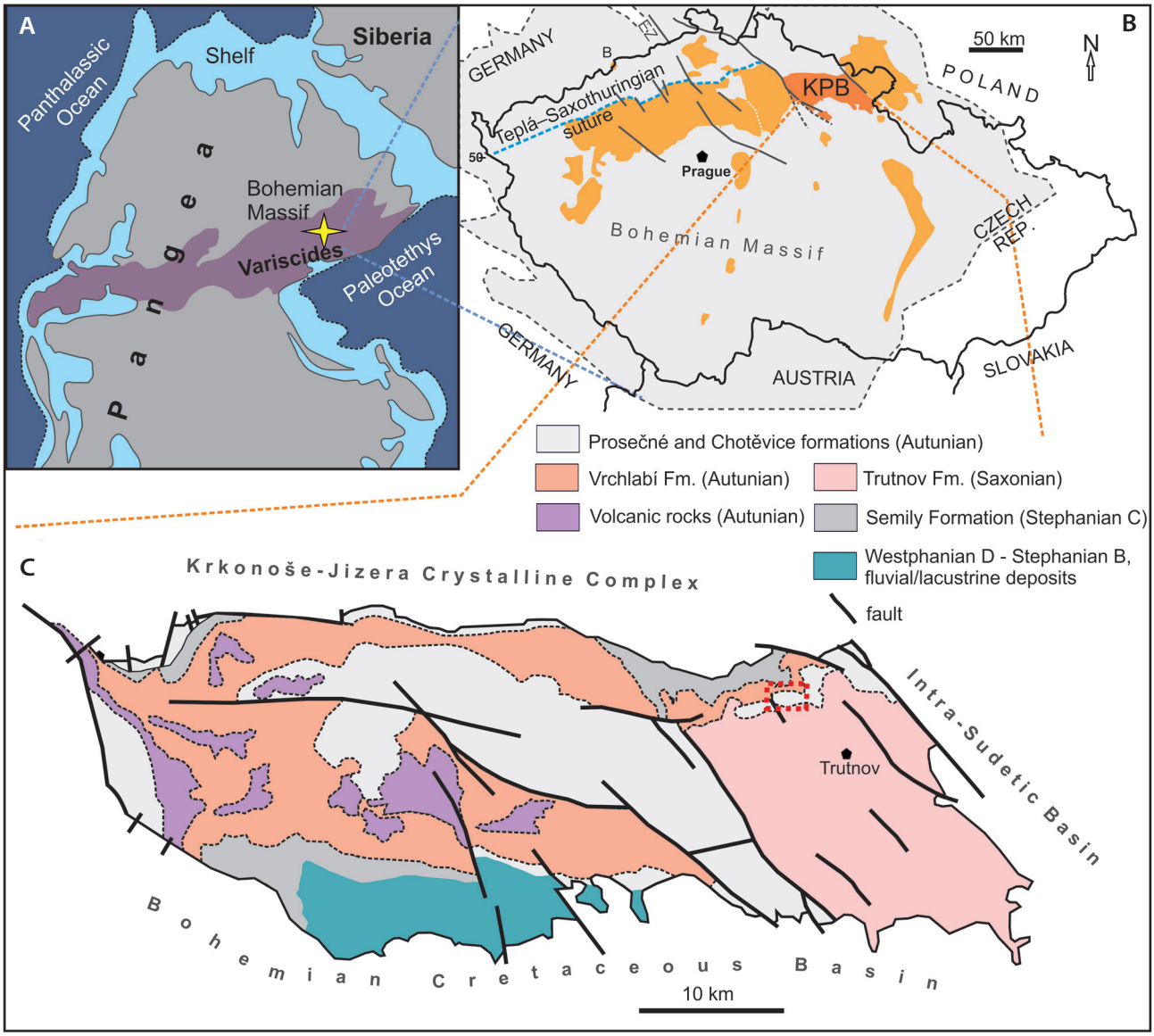

Figure 1. A – palaeogeographic reconstruction of equatorial Pangea showing the approximate position of the Bohemian Massif during the early Permian (*ca*. 280 Ma), modified from Blakey (2020). • B – Carboniferous and Permian continental basins in the Czech Republic, highlighting the Krkonoše Piedmont Basin (KPB, dark orange), modified after Schöpfer *et al*. (2022). • C – geological map of KPB showing structural configuration and regional extent of formations. The studied site near Mladé Buky is marked by a red rectangle. Modified from Martínek *et al*. (2006) and Schöpfer *et al*. (2022).

The sedimentation of the Chotěvice Formation was influenced by progressive aridization, with the environment changing from alluvial plain to a playa-like system (Roscher & Schneider 2006). In the upper part of the Chotěvice Formation, reddish aleuropelites with abundant evaporites were documented (Prouza *et al*. 1977). Locally, colorful claystones and siltstones with tuffitic layers occur (Prouza & Tásler 2001).

The sedimentation of both units was accompanied by andesitic and rhyolitic volcanism, as evidenced by numerous tuffitic layers. In the lower part of the Chotěvice Formation, Tatobity rhyolite ignimbrite body is embedded, which outcrops in the western part of the KPB (Opluštil *et al*. 2016), though its lateral extent remains largely unknown. The rhyolitic volcanism ceased during the sedimentation of the Chotěvice Formation (Prouza & Tásler 2001, Ulrych *et al*. 2003).

Material and methods

Representative large samples were cut transversely and longitudinally and polished (Technistone, Hradec Králové, Czech Republic) to observe macroscopic features. For

microtextural and microstructural observations, both polished thin sections (14; 3 × 4 cm, ~ 50 μm thick) and uncovered, unpolished thin sections (13; 3 × 4 cm, 30 μm thick) were examined. For LA-ICP-MS analysis, two polished thin sections with a thickness of 120 μm were prepared. The thin sections were prepared at the Czech Geological Survey (CGS) laboratory in Prague. The thin sections were scanned using a PrimeHisto XE slide scanner and studied and photographically documented using an Axio Imager A2m Carl Zeiss microscope. For scanning electron microscopy, certain parts of the selected thin sections were etched with 5% hydrofluoric acid (HF) for 10 min in the palynological laboratory of the CGS. This etching process was performed to enhance the visibility of microstructural and microtextural features. A Tescan Mira 3GMU FEG-SEM scanning electron microscope (CGS, Prague) equipped with a couple of energy-dispersive spectrometers Oxford Instruments Ultim Max 100 (active area 100 mm^2) was used for imaging and phase analysis at an accelerating voltage of 15 kV, beam current of 1.8 nA and working distance of 15 mm. The surfaces of the thin sections were covered with a 15 nm thick layer of amorphous carbon to avoid charging. The samples are stored in collections of the Czech Geological Survey (Prague).

Element geochemistry. – Major, trace, and rare earth element (REE) compositions at microscale resolution were determined in two polished thin sections (thickness 120 μm) using laser ablation–inductively coupled plasma-mass spectrometry (LA-ICP-MS) at the Department of Chemistry, Masaryk University, Brno, Czech Republic. For the *in situ* microgeochemical analysis, an Analyte G2 (Photo Machines Inc., Redmond, WA, USA) excimer laser ablation system coupled with a high-resolution sector-field Element2 (Thermo Fisher Scientific, Waltham, MA, USA) ICP-MS was used. The laser operated at a wavelength of 193 nm with a pulse duration ≤ 4 ns. Using helium as a carrier gas with a flow rate of 0.65l min^{-1}, the aerosol was washed out of the chamber (HelEx) and transported through a Fluorinated Ethylene Propylene (FEP) tube (i.d. 2 mm, length 1 m) to the ICP-MS. Ablation was performed as spot analyses with 85 μm diameter size, repetition rate of 10 Hz and 3 J cm^{-2} fluence. The ablation time for each analysis was 60 s. External calibration was based on standard reference materials (SRM) NIST 610 and NIST 612. Owing to sample heterogeneity, internal standardization was replaced by the sum of element oxides for quantification. The total sum of all the oxides (estimated from elemental analysis by LA-ICP-MS) was normalized to 100 wt%. The analytes were expressed as elements in ppm. This method is independent of the internal standard and does not require precise determination of the reference element by another analytical method at the specific area of the ablation spot. The LA-ICP-MS output was evaluated using the Ilaps software, specially developed for LA-ICP-MS data reduction (Faltusová *et al*. 2022).

Concentrations of REE normalized to the average upper continental crust concentrations (UCC; McLennan 2001) are expressed as REE_N (suffix N stands for REEs normalized to UCC). The cerium (Ce/Ce*) and europium (Eu/Eu*) anomalies were calculated following Lawrence *et al*. (2006): $Ce/Ce^* = Ce_N/(Pr_N) \times (Pr_N/Nd_N)$ and $Eu/Eu^* = Eu_N/(SmN\ 2 \times Tb_N)^{1/3}$.

Raman Spectroscopy. – Raman spectroscopy was performed using a JY/Horiba LabRam HR Raman system (Department of Geological Sciences, Masaryk University, Brno, Czech Republic). Raman spectra were calibrated with a silicon wafer. A 532 nm (Nd-YAG) laser with 20/60 mW excitation power was employed for the analyses. Data were collected in the 1000–2000 $cm^{-}1$ range using a diffraction grating with 600 grooves/mm, entrance slit of 200 μm, confocal hole of 400 μm, and 100× Olympus BX-41 objective. The acquisition time was set to 10 s with one accumulation per spectrum.

Optical cathodoluminescence. – Optical cathodoluminescence of one polished carbon coated thin section was studied by using Simon-Neuser HC2-LM CL microscope with "hot cathode" (Department of Geological Sciences, Masaryk University, Brno, Czech Republic). The electron gun operated at 14 kV with a current density of 10–40 μA/mm^2 in a vacuum (10−6 bar). Microphotographs were taken using a digital camera (Olympus C-5060) under cathodoluminescence for longer exposure times (1–10 s).

Biomarker analysis. – Due to the high porosity of the fossil material, the most compact portion represented by the finely-crenulated lamination was selected for analysis to minimize potential contamination.

The elemental composition of total organic carbon (TOC), total inorganic carbon (TIC) and total sulphur (TS) were analysed using an ELTRA® 2000 instrument with three infrared detectors. TIC was measured using a phosphoric acid treatment, while TOC and TS by oxidation in oxygen flow at 1420 °C after the removal of carbonates by HCl at 40 °C. Soluble organic matter was extracted from rocks using a Dionex® accelerated extractor by a DCM–methanol mixture (97 + 3) and the solution volume was reduced by Turbovap. Elemental sulphur was removed by activated copper. Saturated (SAT), aromatic (ARO) and polar (NSO) fractions were separated on a silica column. SAT and ARO fractions were analysed by gas chromatography–mass spectrometry (Agilent 7890A and 5973N MSD). Mass chromatograms were evaluated as peak areas and molecular biomarkers ratios calculated

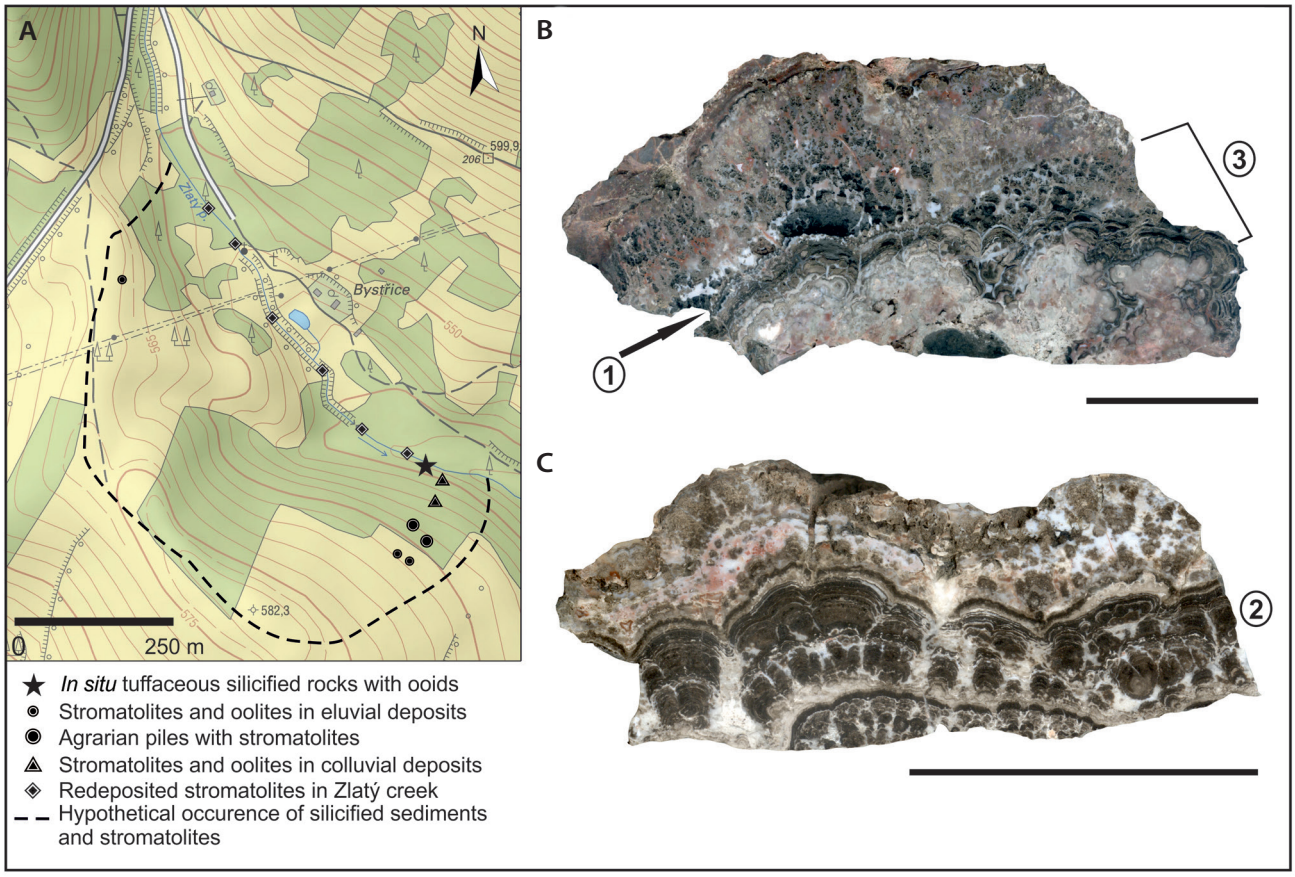

Figure 2. A – geographic map of the sampling site near Mladé Buky a former settlement Bystřice. Location of studied silicified stromatolites and oolites in the Mladé Buky area. Different symbols indicate sampling context as shown in the legend. Agrarian piles represent historical stone accumulations created by field clearing. Base map source: ČÚZK (State Administration of Land Surveying and Cadastre). • B–C – polished stromatolite samples from eluvium, scale = 5 cm. B – arrow 1 shows millimetre-thick laminated interval with ~ 1 mm wide ridges (meso- and macrostructure type 1); area 3 shows juxtaposed columns (~ 1 cm wide) with poorly preserved convex lamination (meso- and macrostructure type 3). C – area 2 shows vertically stacked, closely spaced, and/or juxtaposed millimetre-sized domes (meso- and macrostructure type 2).

using three NIGOGA standards of the Norwegian Petroleum Directorate (NIGOGA 2000).

Terminology used. – Microbialite: Defined by Burne & Moore (1987, p. 241) as follows: "Microbialites are organosedimentary deposits that have accreted as a result of a benthic microbial community trapping and binding detrital sediment and/or forming the locus of mineral precipitation."

Stromatolite: the term is used in the sense of Riding (1991, p. 47) as "laminated, benthic microbial deposit", by using this term the microbial nature of the deposit is implied. The stromatolite morphology is described mainly using the terms from Hofmann (1969), Hofmann & Jackson (1987) and Grey & Awramik (2020).

Ooid: used throughout this paper for smooth, ovoid coated grains (with rocks composed of these grains referred to as oolites). Although some grains exceed the traditional 2 mm size limit for ooids (reaching up to 5 mm), we apply this term consistently because of the similar concentric internal structure and regular and continuous lamination patterns. This simplified terminology avoids arbitrarily size-based distinctions between otherwise identical grains.

Results

Meso- and macrostructures of the stromatolites

Within individual specimens, associations of various stromatolitic structures in vertical succession were observed, although the character of the material (isolated boulders) limits interpretation of larger-scale growth patterns. The structures are represented by (1) a few millimetre-thick laminated intervals with *ca.* 1 mm wide ridges (Fig. 2B), (2) vertically stacked, closely spaced, and/or juxtaposed

millimetre-sized domes (usually less than 1 cm in size), and millimetre-scale columns with indistinguishable internal structures (Fig. 2C), and (3) larger areas occupying structures represented by juxtaposed columns (*ca.* 1 cm in width) with poorly preserved convex lamination, giving the rock a honey-comb appearance (Fig. 2B). The structures are mostly dark brown, reddish, and black. The stromatolitic structures project themselves onto the surface as knobs, giving the samples a cauliflower appearance (Appendix 1.1A, B).

Host rock characteristics

The stromatolites occur as silicified boulders within Quaternary eluvium and colluvium, and the original host-rock lithology is rarely preserved. The observed host rock associated with stromatolites consists of very fine-grained silicified material. In one sample, we observed a sequence from stromatolitic structure through layers containing chaotically arranged, unsorted ooids, to a fine-grained silicified matrix containing probable Charophyte remains (Appendix 1.1C–E).

Microstructures of stromatolites

The studied stromatolites are characterized by a notable absence of detrital components, with SEM-EDS analyses revealing negligible amounts of detrital minerals. Four basic morphological microstructures were recognized, which occurred in close association and were suggestive of vertical succession.

(1) Finely-crenulate lamination (Fig. 3A–F), which corresponds to meso- and macrostructure type 1, consists of alternating dark (dense) and light (porous) laminae, typically only a few millimetres thick. The laminae appear to merge into anisopachous layers approximately 50–100 μm thick. The light laminae characteristically thicken in the crestal areas of convex, irregular fine ridges. Observations of polished and HF-etched thin sections under crossed polarized light reveal grain size differences between dark and light laminae (Fig. 3E). Light laminae contain coarser (≥ 10 μm) anhedral, equant SiO_2 microcrystals, while darker laminae comprise fine-grained (< 6 μm) equant crypto-microcrystalline SiO_2. Although preservation limits the assessment of lateral continuity, lamina can typically be traced for several millimetres, with laminae of identical colour and specific fabric traceable between adjacent fine ridges.

The laminar profiles range from slightly undulating to steeply convex, with the latter showing moderate synoptic relief. The lamination demonstrates a relatively high inheritance, with successive laminae mimicking the morphology of the underlying laminae. The irregular fine ridges are variably spaced and predominantly open-spaced. This type of microstructure occurs in vertical succession with the other structures, as shown in Fig. 3F.

Interpretation: The silicification pattern appears to preserve the original carbonate microtexture, where the darker fine-grained layers likely represent former micritic lamination. What appears to be more porous layers, now formed by coarser-grained SiO_2, could represent primary porosity of the stromatolites, filled with early carbonate cement (later replaced by SiO_2). Considering the characteristic thickening of the lighter laminae at the crestal areas of the miniridges, it seems more probable that these areas represent zones of enhanced carbonate precipitation due to the metabolic activities of the microorganisms. While various microbial metabolic pathways can drive carbonate precipitation in stromatolites (Dupraz *et al*. 2009), the preferential precipitation in crestal areas suggests that photosynthesis was the dominant mechanism here, as these areas would receive maximum light exposure. Donaldson (1976) and Bosak *et al*. (2009) described similar crestal thickening in conical stromatolites, interpreting it as a result of photosynthetic bubble formation. Although bubble formation is a plausible mechanism, the systematic pattern of thickening following the crests in our samples is more consistent with enhanced carbonate precipitation driven by photosynthetic activity. However, we acknowledge that without the knowledge of the stratigraphic position and orientation of these samples, this interpretation regarding photosynthetic influence remains tentative.

(2) Contiguous thinly laminated domes with a gently convex laminar profile (Fig. 3G–L), which corresponds to meso- and macrostructure type 2. The microlamination appears to consist of repetitive layers, each 50–100 μm thick, showing a distinct pattern (Fig 3J–L): (1) a layer of relatively coarse-grained (~ 40 μm) equant anhedral SiO_2 crystals, (2) a layer formed by vertically oriented, elongated SiO_2 crystals (*ca.* 1–5 μm wide and up to 40 μm long), and (3) a very thin layer with a concentration of openings that were wide from a few microns up to 50 μm, which followed the horizontal laminations

Interpretation: While the preservation limits interpretation, the regular, vertical needle-like crystals may represent former carbonate cement growing between horizontal microbial laminae, now preserved as openings containing organic matter and iron oxides. This pattern could reflect cyclic development of microbial mats followed by cement precipitation. Similar cyclic textural development was described in travertines by Okumura *et al*. (2013a, b) and interpreted as daily lamination, where microbial layers form during the day and inorganic

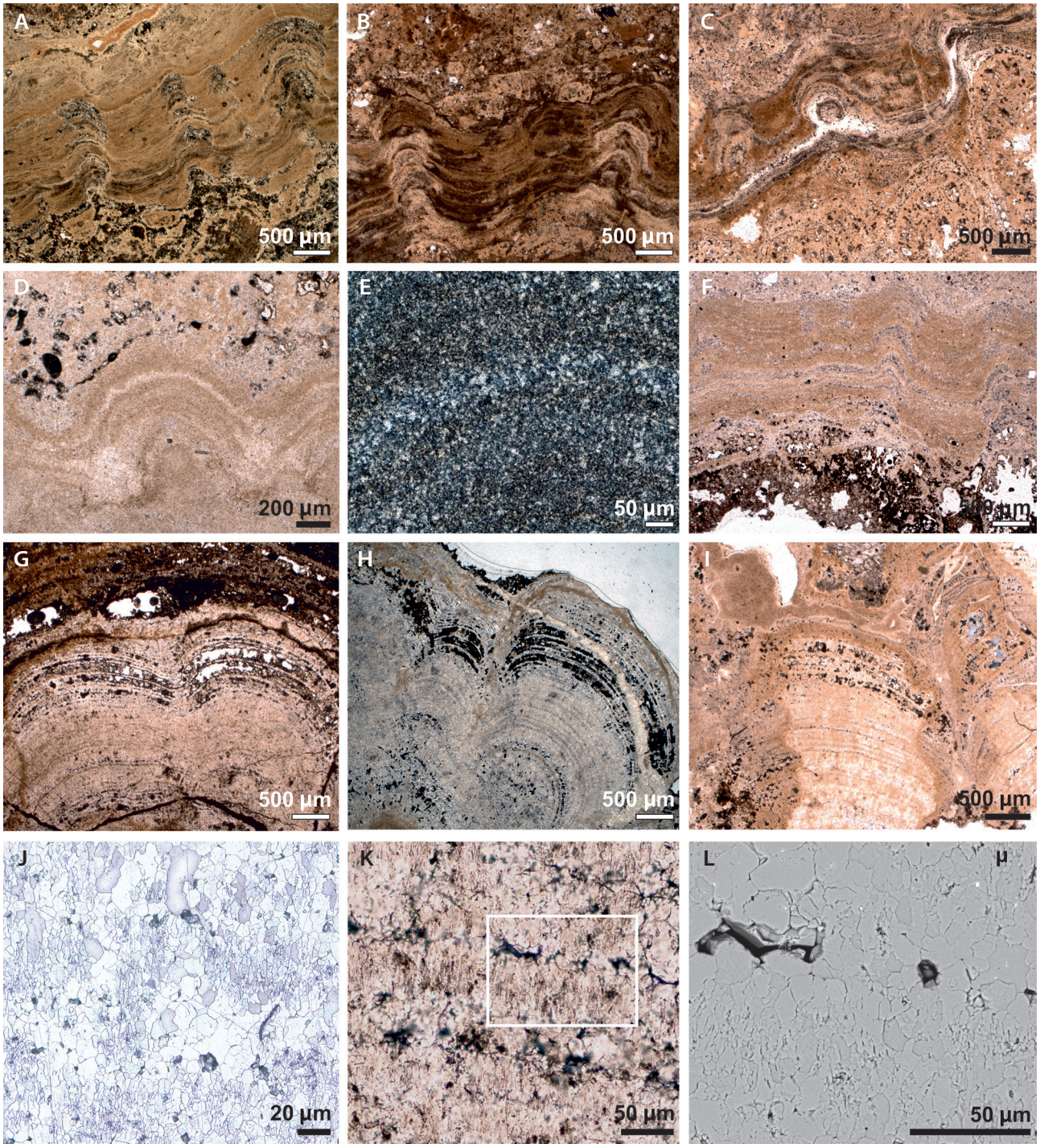

Figure 3. A–F – photomicrographs showing finely-crenulate lamination (microstructural type 3) featuring alternation of dark and light laminae with characteristic thickening in the crestal areas [A–D, F: transmitted light images; sample numbers: A: 567, B: 976 (HF etched), C: 976, D–E: 971]. E – cross-polarized light photomicrograph showing detail of fine ridge crest from D. Light, coarser laminae consist of equant microcrystalline quartz, while darker areas comprise crypto-microcrystalline equant quartz. F – vertical association of microstructure type 4 (poorly preserved closely-spaced minicolumns with gently convex laminations, darker area at the bottom of the image) and finely-crenulate lamination (sample 969). • G–I – transmitted light photomicrographs of microstructure type 2 showing contiguous thinly laminated domes with gently convex laminar profile [sample numbers: G: 565 (HF etched), H: 565a, I: 566]. • J–L – details of microlamination in H, illustrating cyclic arrangement of layers (coarser-grained equant anhedral SiO_2 crystals alternating with vertically oriented elongated SiO_2 crystals and thin layers with lamination-parallel openings). J – reflected light image, K – transmitted light image, L – BSE image of detail marked in K.

calcium carbonate precipitation occurs during the night, covering the microbial layer.

Very similar structures were documented by Frantz *et al*. (2014) and figured in Grey & Awramik (2020, fig. 121c therein) from the lacustrine Tipton Member of the Green River Formation (Eocene, Wyoming, USA).

(3) Radial fans (Fig. 4), correspond to meso- and macrostructure type 2. These contiguous microstructures, measuring up to 2.5 mm in width and 2.8 mm in height, exhibit hemispheroidal, fan- and club-like shapes, are adjacent, and are often vertically stacked (Fig. 4A–F), or form layers with palisade-like fabric (Fig. 4G). These microstructures comprise two distinct morphotypes. The first type is characterized by abundant elongated openings (20–100 μm long, 20–50 μm wide) that radiate upward and outward in a fan-like pattern and are intersected by horizontal opening alignments (Fig. 4A, B, D, E). This morphotype exhibits indistinct, irregular, convex horizontal lamination (Fig. 4B, D, E). The second type shows similar upward and outward radiating pores but lacks the apparent horizontal pore alignments (Fig. 4C, F, G) and features two lamination patterns: an indistinct irregular horizontal lamination similar to the first morphotype (Fig. 4C, G), and a distinctive microlamination identical to that observed in microstructure type 2 ('Contiguous, thinly laminated domes'; Figs 3K, 4F).

Interpretation: Structures similar to 'radial fans' are known from various recent sedimentary environments, such as lacustrine (*e.g*. Schäfer & Stapf 1978, Golubić *et al.* 2008), hot springs, and geyser geothermal areas (*e.g*. Fernandez-Turiel *et al*. 2005, Munoz-Saez *et al*. 2016, Murphy *et al*. 2021), peritidal (*e.g*. Smith *et al*. 2005) and especially from rivers and streams (*e.g*. Howe 1932; Monty 1976; Freytet & Plet 1991, 1996; Freytet & Verecchia 1998; Caudwell *et al*. 2001; Pitois *et al*. 2001; Hägele *et al*. 2006; Rott *et al*. 2012; Tran *et al*. 2019), where they were recognized as shrubs composed of calcified dense filaments of cyanobacteria, most commonly assigned to the genera *Phormidium*, *Oocardium*, *Rivularia*, and *Schizothrix*, which characteristically grow perpendicular to the surface, thus forming radially arranged fans. Comparable structures interpreted to be of microbial origin are also known from the Proterozoic (Cao 1991, Kah & Knoll 1996, Bartley *et al*. 2000), Mid-Palaeozoic thermal springs (Walter *et al*. 1998), lacustrine Permian deposits (Schäfer & Stapf 1978, Hellwig *et al*. 2023) and Jurassic hot springs (Cambell *et al*. 2015, Guido *et al*. 2019), non-marine Cretaceous (Monty & Mas 1981, Dragastan & Mišík 2001) and Miocene lacustrine deposits (Willmer & Rasser 2022), Quaternary lacustrine (Casanova & Hillaire-Marcel 1992) and fluvial deposits (Janssen *et al*. 1999, Kleinteich *et al*. 2017). We have no intention of assigning the forms observed herein to a particular texonomic group. However, certain interpretations can be made based on our observations. The openings exhibited distinct patterns of both vertical and horizontal alignments (Fig. 4A, B, D, E), while some display exclusively horizontal arrangements (Fig. 4C, G). The size and spatial organization of these openings are remarkably similar to the distribution patterns of cells or chains of cells of modern sheath-forming cyanobacterial colonies, particularly those forming fan-like and hemispheroidal growth forms (see references above). We hypothesize that the structures observed herein were formed by sheath-forming cyanobacterial taxa forming fan-like and hemispheroidal colonies with characteristic upright growth perpendicular to the surface. The polysaccharide sheaths not only surrounded the cyanobacterial cells but also entire colonies, and we interpret the horizontal lamination of brownish colour in Fig. 4B–D, G (arrows) to represent such microstructures, that were calcified and eventually silicified. The indistinct lamination within the colonies most likely represents periodic growth phases of the cyanobacterial colony.

(4) Closely-spaced minicolumns with gently convex laminations (corresponding to macrostructure no. 3) (Fig. 5). These microstructures form adjacent columns, each approximately 5 mm wide and 10 mm high, and always exhibit poor preservation. The remnants comprise gently convex laminae forming what appears to be a reticulate pattern, with extensive void spaces (now resin-filled) between the preserved material. These poorly preserved columnar structures occur in vertical association with other microstructures, as exemplified in Fig. 5A, where finely-crenulate laminated microstructure occurs between the columnar structures (see also Fig. 3F). SEM-EDS analysis indicates that, in addition to SiO_2 and iron oxides, manganese oxides associated with organic matter are the main components (see Results, 'Scanning electron microscopy and EDS analyses of the stromatolites').

Figure 4. Microstructure type 3, Radial fans, shown in thin section scan (A) and photomicrographs in transmitted light (B–G). A – overview with rectangles 1 and 2 corresponding to B and D, respectively (sample 973). A–F – adjacent hemispheroidal, fan and club-like forms. B, D–E – cyanobacterial colonies displaying cyclic growth phases (visible as indistinct internal lamination) and brownish laminated envelopes (arrows) interpreted as primary calcified mucilage (polysaccharide sheaths). Note both vertical and horizontal alignment patterns of openings interpreted as remains of cyanobacterial cells (E: sample 975). C – hemispheroidal cyanobacterial colony showing vertically aligned openings and calcified (subsequently silicified) mucilage enveloping the entire colony indicated by arrow (sample 568). F – detail of C showing microlamination comparable to Fig. 3J–L. G – continuous, palisade-like form of cyanobacterial colony (sample 568).

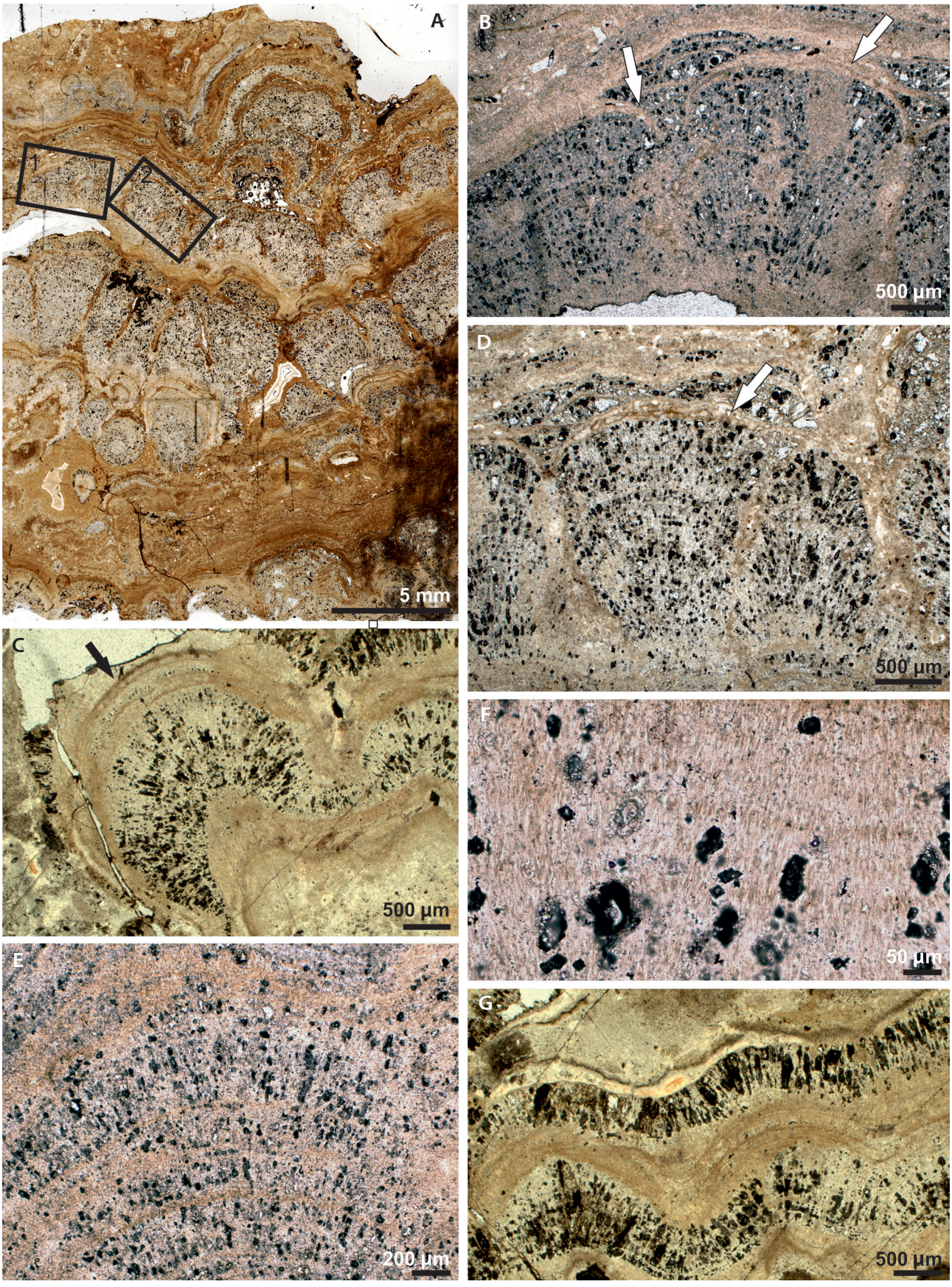
A
1
2
5 mm
B
500 µm
C
500 µm
D
500 µm
E
200 µm
F
50 µm
G
500 µm

Interpretation: While diagenetic processes can produce Mn oxide precipitates, the restricted occurrence of these distinctive filamentous networks specifically within 'closely-spaced minicolumns with gently convex laminations', rather than being distributed evenly throughout all microstructures, suggests potential biological influence in their formation (Mn oxides were also identified within the openings of microstructure types 1–3, however, occurring in minor amounts). Notably, a consistently poor preservation was observed exclusively in Mn oxide-rich portions of the stromatolites, which may reflect degradation in localized anoxic microenvironments within the structures, likely created by organic matter decay, where manganese remobilization occurred prior to silicification. However, without comparable structures in either modern or fossil examples, and considering possible post-depositional modification, a conclusive interpretation of the role of manganese oxides in these structures remains elusive.

Oolites and oolitic rocks

Along with stromatolites within the Quaternary eluvium and colluvium, Permian oolites and silicified rocks containing ooids have also been documented. The oolites occur in two distinct facies: (1) laminated deposits with bimodal sorting, where ovoid ooids show alignment of their long axes parallel to the bedding plane (Fig. 6A), and (2) poorly sorted packstones with chaotically arranged ooids (Fig. 6B, C). Despite the fact that silicification obscures details, signs of pressure solution at grain contacts can be observed (Fig. 6A, C). While stromatolites and oolites typically occur as isolated boulders within eluvium and colluvium, two samples from the eluvium exhibit co-occurrence of stromatolites and ooids (Appendix 1.1D, E). In addition, silicified rocks showing beds of unsorted ooids within a tuffaceous matrix were discovered *in situ* in an excavated creek bank section of limited extent, however, devoid of stromatolites (Fig. 6D, E). Rare silicified land plant remains were also documented within these deposits.

Ooids across all facies ranged from 0.5 to 2 mm in diameter, occasionally reaching 5 mm. The grains are smooth, oval in cross-section, and, if well preserved, display concentric laminated microstructure. The lamination consists of alternating darker, micro-cryptocrystalline quartz bands and lighter, microcrystalline quartz bands. Although most nuclei are obscured, several types have been identified: (1) elongated, dark brown carbonaceous remains (probable phytoclasts) that determine the ovoid shape of the ooids (Fig. 6B, C), (2) isotropic, glassy groundmass with brown alteration rims (Fig. 6D). The latter also occurs within the ooidal cortex and within the matrix of oolitic rocks found in situ in the excavated creek bank section (Fig. 6D, E). Importantly, in samples of oolites from eluvium, euhedral sanidine crystals were recorded both in the oolite matrix and within ooidal cortices, where they were aligned along ooidal lamination (Fig. 6F). The presence of sanidine was confirmed by XRD analysis (Appendix 1.2).

Scanning electron microscopy and EDS analyses of the stromatolites

The observed microstructures are characterized by openings that show horizontal alignment (microstructures type 1 and 2), both horizontal and vertical alignment, or vertical alignment only (microstructure type 3, Fig. 7A). SEM and EDS analyses of the openings revealed three types of C-rich microstructures: irregular masses (Fig. 7B), organized, net-like structures (Fig. 7C–E) and less commonly filamentous, thread-like forms (Fig. 7F–H). All of these types can occur within the same microstructural type (*e.g.* within 'radial fans'), showing no preferential distribution pattern among different microstructure types. In the thin section etched by HF, a continuous C-rich filament was observed within microstructure type 1 (Fig. 7I). The organic nature of these microstructures is confirmed by EDX spectra, which show C peaks that exceed the intensity typically associated with carbon coatings, as well as the Raman spectroscopy results. EDX spectra further suggest that the organic matter was permineralized by silica. Given that the opening dimensions exceed the EDX interaction volume and SiO_2 was consistently detected in EDX analyses at 15 kV, the Si signal is interpreted to originate from the silica-permineralized organic matter itself rather than from the surrounding siliceous matrix (see Appendix 2, EDX spectra for Fig. 7H). In close association with these C-rich, silica-permineralized microstructures, several other mineral phases were observed: submicron – micron-sized Fe oxides and partly oxidized pyrites (most common, Fig. 7A–C), grains of a chromite-like composition (Fig. 7D), Ti-oxides (Fig. 7H), and Fe-K-Mg aluminosilicates (Fig. 7I). Additionally, a phase showing elevated contents of Mn, Al, Fe, K, and Mg (apart from Si), along with high C peaks and minor amounts of S, P, and Ti was observed (Fig. 7H); however, because of its size, it is unclear whether the phase represents Mn-Fe-K-Mg aluminosilicate or Mn oxides associated with Fe-K-Mg aluminosilicates. Microstructure type 4, 'Closely-spaced minicolumns with gently convex lamination' is characterized by the association of Mn oxides, organic matter, and REE phosphate minerals with compositions consistent with monazite-(Ce), Fig. 8A–C. The Mn oxides form networks of extremely fine, hair-like

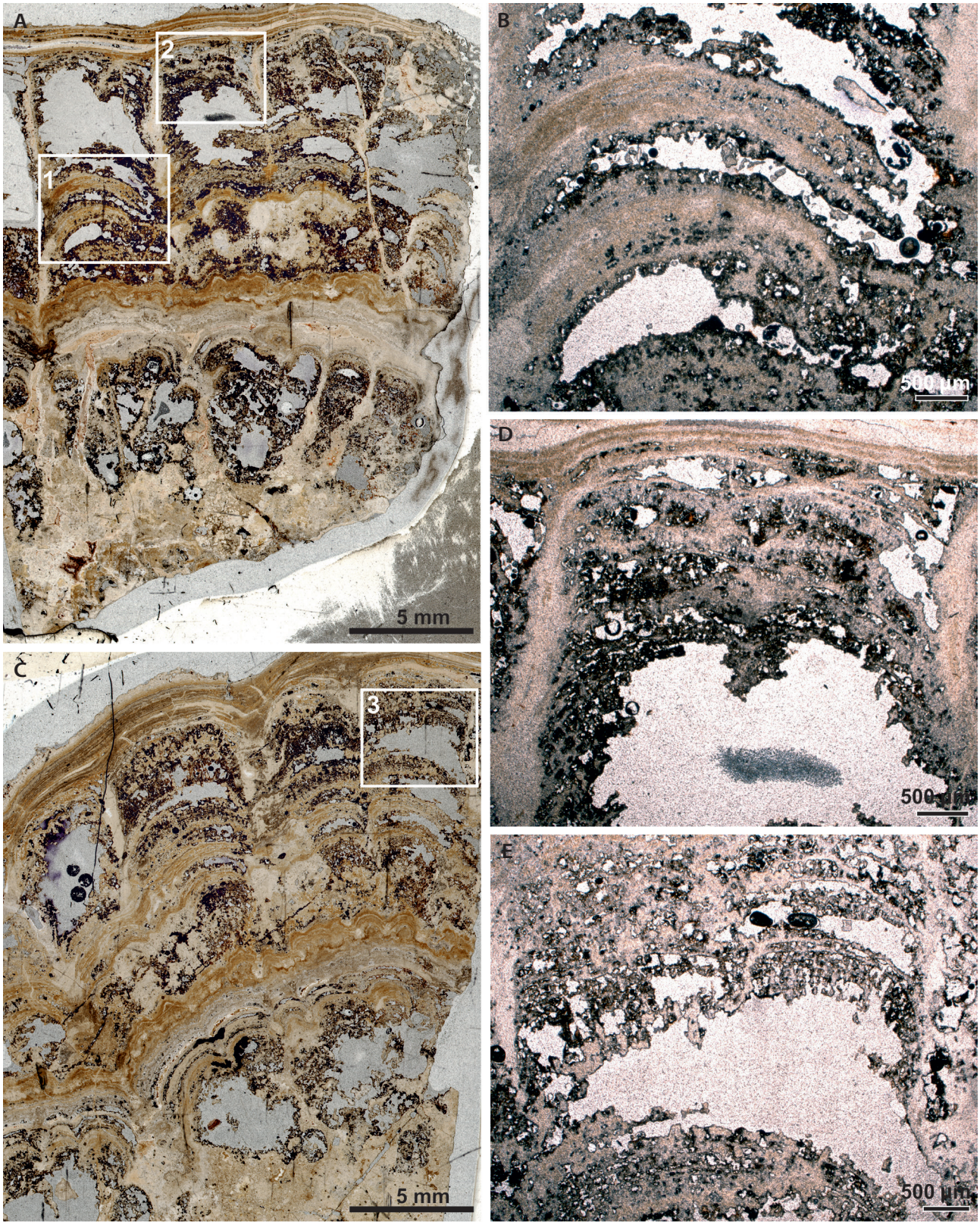

Figure 5. A–E – microstructure type 4 showing closely-spaced minicolumns with gently convex laminations. A, C – thin section scans showing overview of poorly preserved columnar structures (~ 5 mm wide) with extensive void spaces (white areas), and vertical association with minicrenulate lamination between columns in the central part of the images (A: sample 970, C: sample 971). Rectangles 1–3 mark locations of detailed views B, D and E, respectively. B, D–E – details of reticulate pattern formed by gently convex laminae. Dark areas are composed of Mn oxides.

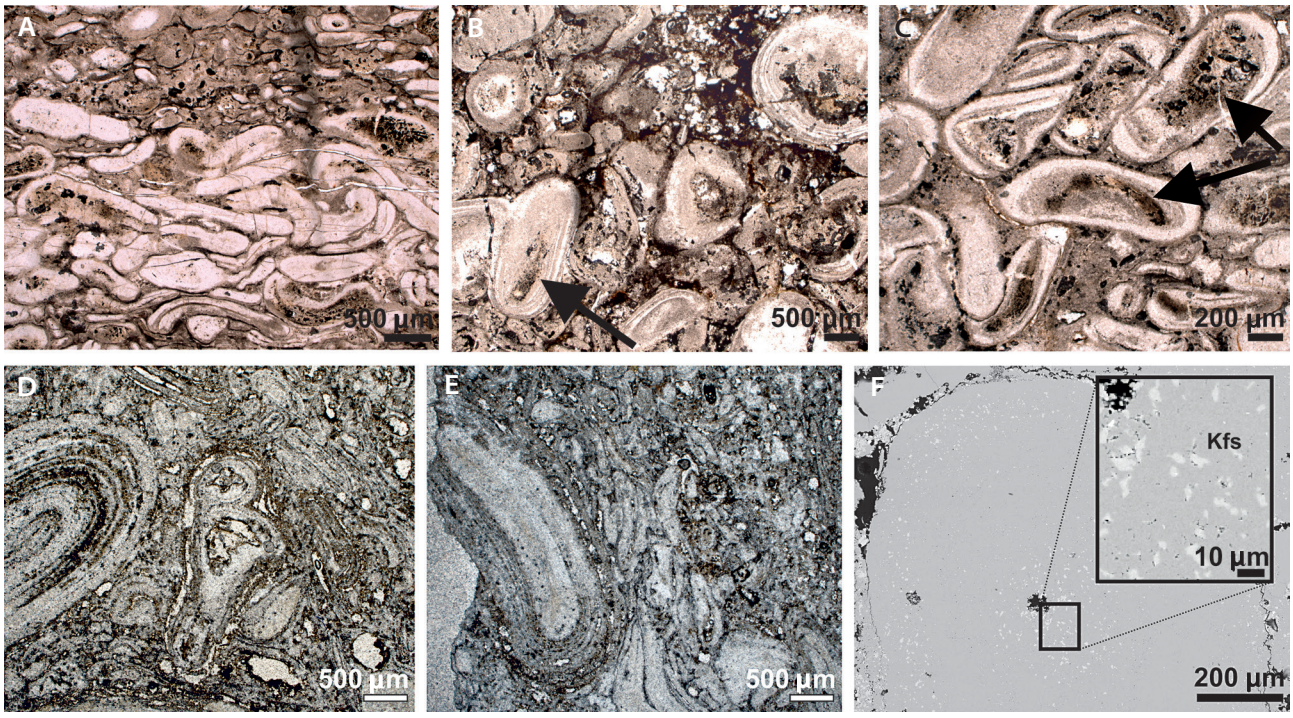

Figure 6. A–F – microphotographs of eluvial and in situ silicified oolites and oolitic rocks. A – eluvial sample showing densely packed oolites with bimodal sorting and longitudinal axes of ooids oriented parallel to bedding (sample 160). B – eluvial sample exhibiting poorly sorted ooids with chaotic arrangement; arrow indicates an ooidal core formed by a phytoclast (sample 161). C – higher magnification view of facies shown in B, with arrows indicating phytoclasts serving as ooidal cores (sample 161). D – *in situ* sample of tuffitic silicified rock containing ooids, featuring grains composed of glassy groundmass and brown alteration rims both as cores and within a cortex of a compound ooid (centre), as well as within the matrix, *e.g.* in the lower right corner (sample 980). E – detail showing grains of glassy groundmass with brown alteration rims occurring within ooidal cortex and matrix (sample 980). F – BSE image of eluvial oolite showing K-feldspar (sanidine) crystals aligned along ooidal laminae (sample 161).

filaments that interweave and branch, creating a delicate mesh-like microstructure. Monazite-(Ce) crystals are randomly distributed throughout this filamentous network, ranging in size from submicron to several micrometres (Fig. 8B, C). Mn oxides were also identified within the openings of microstructure types 1–3, occurring in minor amounts (< 3 wt%) (Fig. 7H).

Silicification patterns and textures

Petrographic analysis of the thin sections under cross-polarized light revealed multiple generations of silicification. The earliest silicification phase, consisting of micro- to cryptocrystalline quartz, preserved the original microtexture (mimetic silicification *sensu* Manning-Berg & Kah 2017) as well as micro- and macrostructures (Figs 3E; 9A–C, F). The later silicification phase is characterized by void- and fracture-filling precipitates, including fibrous quartz (Fig. 9D) and spherulitic chalcedony (Fig. 9E) along cavity and fracture margins, with equant mega-quartz crystals occupying the central portions of these cavities (Fig. 9E). The fracture boundaries where they intersect with the stromatolites are very sharp (Fig. 9D). The third generation of fractures crosscuts both the stromatolites, later fractures and voids but has no precipitation infill.

Element geochemistry

In the stromatolitic structure type 1 ('finely-crenulate lamination'), spots were ablated by LA-ICP-MS system in dark and light laminas, matrix recrystallized in fibrous quartz, and cements (spherulitic chalcedony, fibrous quartz and equant mega-quartz crystals). A sample with stromatolitic structure type 4 ('closely-spaced minicolumnar structures') was selected for the analysis of Mn-bearing dark laminas, "regular" dark and light laminas, and matrix (fibrous quartz).

Because the studied material was siliceous rock, SiO_2 predominated at most of the measured points (median = 98.81%), demonstrating almost complete silicification of the original carbonate (median $CaCO_3$ = 0.33%). However, several ablated spots with a predominant carbonate composition (40–97.63% $CaCO_3$) provide geochemical evidence of the primary carbonate composition. Residual carbonate bearing Mg (8 to 15%) was found in the dark

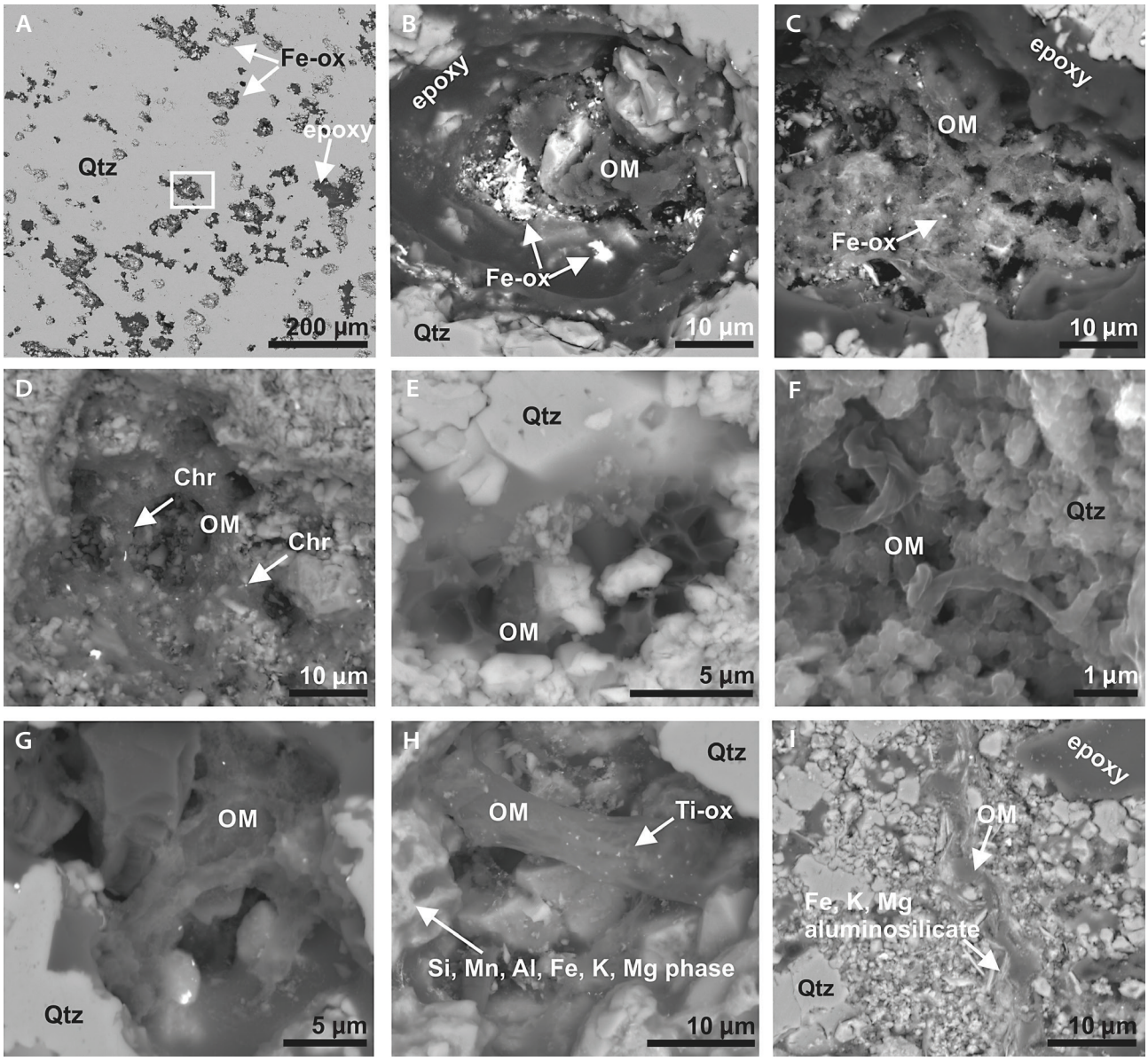

Figure 7. A–E, G–I – BSE images of organic compounds within stromatolitic structures and SE image (F). A – vertically aligned openings in microstructure type 3 (radial fans) showing iron oxides within openings and epoxy resin along opening rims (sample 568). B – detail of rectangular area in A showing iron oxides associated with irregular masses of silica-permineralized organic matter. C – opening within microstructure type 2 (contiguous, thinly laminated domes) displaying organized, net-like, silica-permineralized organic structures with sub-micronic iron oxides. Lighter BSE contrast of silicified organic matter indicates $CaCO_3$ content (sample 565). D – organized, net-like silica-permineralized organic structure with submicronic Cr oxide grains within opening of microstructure type 1 (finely-crenulate lamination) (sample 566). E – polygonal, silica-permineralized organic matter within opening of microstructure type 1 (sample 979). F – SE image showing filamentous structure within opening of microstructure type 3 (sample 976). G – thread-like silica-permineralized organic structure in opening of microstructure type 3 (sample 976). H – thread-like silica-permineralized organic structure within opening of microstructure type 1 (sample 979). I – thread-like silica-permineralized organic structure associated with microstructure type 1, showing association with authigenic aluminosilicates (sample 979). Abbreviations: Qtz – quartz; Fe-ox – iron oxides; OM – organic matter; Chr – mineral of chromite-like composition; Ti-ox – Ti oxides.

laminar parts of the stromatolite. A comparison of the median trace elements concentrations of the samples with the average element composition of the upper continental crust (UCC; McLennan 2001) reveals paucity in lithophile refractory elements (Al, med = 1905.00 ppm; Ti, med = 85.10 ppm; Zr, med = 4.84 ppm), redox sensitive elements (Mn, med = 46.90 ppm; Fe, med = 454.44 ppm; V, med = 8.77 ppm; Zn, med = 5.79 ppm; Cu, med = 12.51 ppm; Ni, med = 2.47 ppm), and biophile trace elements (P, med = 261.25 ppm; Ba = 25.50 ppm) for most of the measured spots. Besides carbonate, several spots in the dark stromatolite laminas are enriched in P (0.07–0.4 %) or

in Mn (0.07–9.79%), both accompanied by increased concentrations of V, Co, Cu, Ni, and Zn.

The analyzed components differ from each other in element composition, especially cements (including the matrix) and stromatolite parts, but differences can also be traced among individual types of cements and dark-, light-, and Mn-bearing stromatolite laminae (Fig. 10A). Cements are characterized by systematically higher Si/Al ratios, with very low contents of Al, Ca, and Fe (Fig. 10A). The latest equant mega-quartz cement in the central part of the cavities exhibits highly variable concentrations of Zn and P, which are very low in the late fibrous quartz and spherulitic chalcedony cements (Appendix 1.4). The matrix has similar ranges of element concentrations as fibrous quartz and spherulitic chalcedony cements and can be geochemically discriminated from them only by the higher Zr content (Fig. 10A). Stromatolite has higher to very high Ca (highest in the dark laminas), Al and Fe contents (Fig. 10A). The dark laminae revealed the presence of Mn (Fig. 10A) and Zn enrichment, particularly in the Mn-bearing laminae in the structure type 4 ('closely spaced minicolumns structures'), which are also enriched in Ba, Ni, Cu, and Zn (Appendix 1.4). Vanadium was enriched in the dark and light areas of structure type 1 ('finely-crenulate lamination') (Appendix 1.4). The values of V/Cr range between 0.10 and 67.32 (median 2.13).

Systematic differences in the REE composition among the studied components were also observed. REE content varies distinctively between 0.07 and 929 ppm in the studied samples (median 25.18 ppm); cements and matrix show very low concentrations (median 1.97 ppm), while the stromatolite parts are REE enriched (median 52 ppm) (Fig. 10A). Cements and stromatolite also differ in the pattern of REE normalized to the UCC (McLennan 2001). Light-REE (LREE; La, Ce, Pr, Nd) depleted and heavy-REE (HREE; Ho, Er, Tm, Yb, Lu) enriched pattern was measured in cements and in several stromatolitic laminas (Fig. 11A), whereas most of the measured spots in the stromatolite show a middle-REE (MREE; Sm, Eu, Gd, Tb, Dy) enriched pattern (Fig. 11B, C). The spots ablated in the matrix exhibit both patterns. The third type of REE pattern is LREE-enriched/HREE-depleted, which was measured from several spots in the stromatolite (Fig. 11D). Cerium anomalies (Ce/Ce*) range between 0.01 and 9.29 (median 0.99) and Eu anomalies (Eu/Eu*) between 0.12 and 13.87 (median = 1.09). Y/Ho values are mostly superchondritic (median 30; mostly above 33) in stromatolite and fibrous quartz and spherulitic chalcedony cements, whereas the latest equant mega-quartz cement is distinguished by very low Y/Ho (median 12).

Interpretation: Silicification was pervasive as evidenced by the composition of the majority of ablated spots. The degree of silicification is well displayed by Si/Al showing the highest values (and highest degree of silicification) in late cements, lower in early cements and matrix, and the lowest values in stromatolitic laminae (Fig. 10A). Some places were not affected by silicification to such an extent and the carbonate composition was preserved, specifically in the dark laminae of the stromatolite. The high amounts of $CaCO_3$ and Mg revealed the dolomitic composition of the carbonate. A statistically significant correlation with high correlation coefficient between the sum of the REE content and Ca ($r_s = 0.83$, $n = 57$, $p < 0.001$) and Mn ($r_s = 0.61$, $n = 57$, $p < 0.001$) revealed the prevailing REE sources in the carbonate and Mn phases. The additional REE-bearing phases are phosphates, as P shows a significant medium positive correlation with REE content ($r_s = 0.54$, $n = 57$, $p < 0.001$). The UCC-normalized REE pattern of stromatolitic parts show predominantly MREE enrichment in both Si-, Ca-, and Mn-rich spots (Fig. 10B, C; Appendix 1.5). Based on the relationship between REE and other elements mentioned above, the patterns showing "MREE-bulge" can be attributed to the desorption of the MREE-enriched solid Mn oxides under early suboxic conditions and adsorption of the MREE to the early diagenetic phosphates (*e.g*. Haley *et al*. 2004, Paul *et al*. 2019). Additionally, MREE enrichment could be affected by the biological activity of bacteria and algae (*e.g*. Paul *et al*. 2019, Yang *et al*. 2017) and this influence cannot be ruled out due to the context of origin of the stromatolites. Part of the geochemical signal of stromatolite is also related to preserved organic matter, as evidenced by the LREE-enriched pattern, which is typical of organic matter hosted in black shales (Pi *et al*. 2013, Bai *et al*. 2015). The LREE-depleted/HREE-enriched pattern prevailing in all types of cements and occurring in the dark laminae of stromatolite microstructure type 4 is surprisingly similar to the pattern of seawater and its precipitates, which are additionally characterized by positive La, Eu, and Y anomalies and negative Ce anomalies (*e.g.* Deng *et al*. 2017). However, similar patterns have been documented even in lacustrine stromatolites (Zeyen *et al*. 2021). However, unlike the seawater pattern, cements and laminae in the studied sample show predominantly positive Ce anomalies, accompanied by weak positive Eu anomalies; positive Ce and Eu anomalies are typical for sediment precipitation under extremely reducing and alkaline conditions (Bau *et al*. 1996, Garnit *et al*. 2012), while positive Eu anomalies are related to reductive hydrothermal fluids (*e.g*. Bau 1991, Jiang *et al*. 2015) or can be inherited from dissolved feldspars (Shields & Stille 2001). A comparison of the elemental compositions with published examples does not provide convincing evidence for the important influence of hydrothermal fluids. A plot of Ce anomalies *vs.* Y_N/Ho_N (Bau *et al*. 2014) for the discrimination of Mn-Fe precipitates origin shows mostly the hydrogenetic and diagenetic composition of Mn precipitates, although one

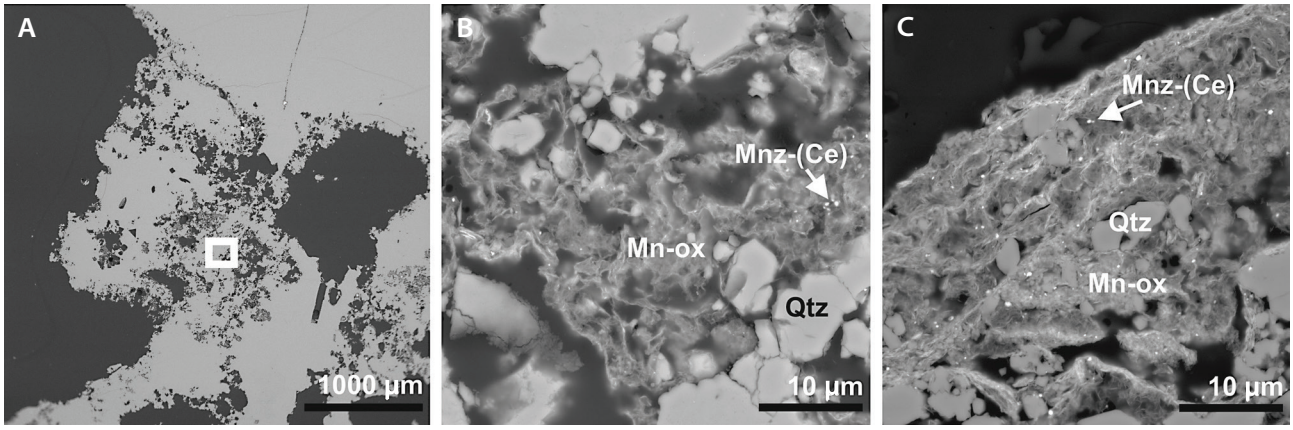

Figure 8. A–C – BSE images of microstructure type 4 (closely-spaced minicolumns with gently convex laminations). A – overview image exemplifying poor preservation of structures associated with Mn oxides (sample 568). B – detail view of rectangular area in A showing hair-like Mn oxides associated with organic matter and submicron-sized Ce monazite. C – filamentous and hair-like Mn oxides associated with organic matter and submicron-sized Ce monazite (sample 569). Abbreviations: Qtz – quartz; Mn-ox – Mn oxides; Mnz-(Ce) – Ce monazite.

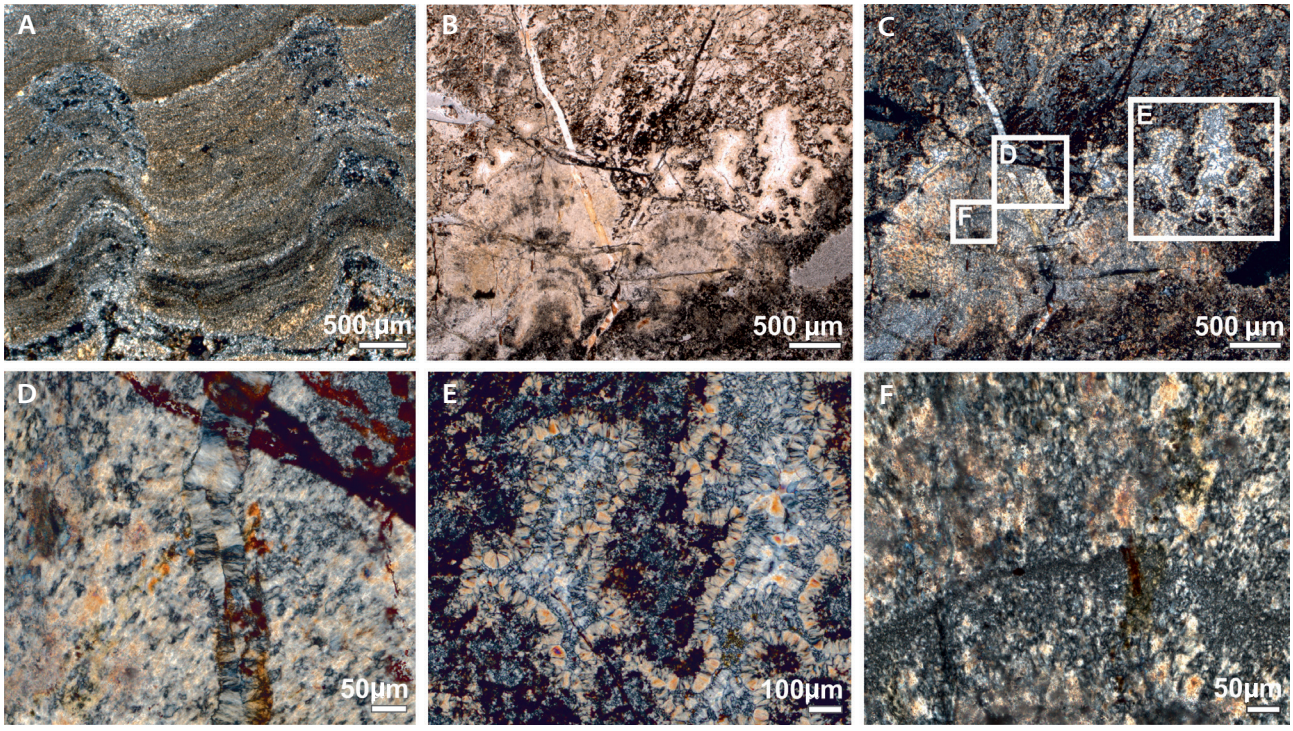

Figure 9. A–F – microphotographs showing early (A–C, F) and late (D, E) silicification patterns. A, C–F – crossed-polarized light images, B – transmitted light image. A – closeup of two fine ridges from Fig. 3A showing alternation of crypto-microcrystalline equant quartz crystals (brownish laminae) and coarser-grained microcrystalline quartz crystals, mimicking original carbonate texture of micritic laminae and early carbonate cement (sample 567). B, C – poorly preserved radial fans exemplifying early and late silicification phases (sample 165), C shows rectangles marking locations of higher magnification views shown in D, E, and F. D – vertical fracture crosscutting the radial fan structure, infilled by fibrous quartz growing perpendicular to the fracture wall. E – void with first-generation spherulitic quartz growing on the walls, followed by second-generation spherulitic mega-quartz infill. F – laminae formed by crypto-microcrystalline equant quartz crystals mimicking former carbonate micritic layer.

spot matches with hydrothermal values (Appendix 1.6A). On the other hand, biplot Eu/Eu* *vs.* Y/Ho for assessing proportions of sea water, hydrothermal fluids and river water (Gao *et al*. 2020) shows prevailing composition close to the river water with some degree of mixing with hydrothermal fluids (Appendix 1.6B). Therefore, the evidenced LREE-depleted/HREE-enriched pattern with weak positive Ce and Eu anomalies seems to be most likely inherited from primary carbonate precipitated under reductive and alkaline conditions, with limited influence of hydrothermal fluids. Reducing microenvironmental conditions are further evidenced by high V/Cr values at

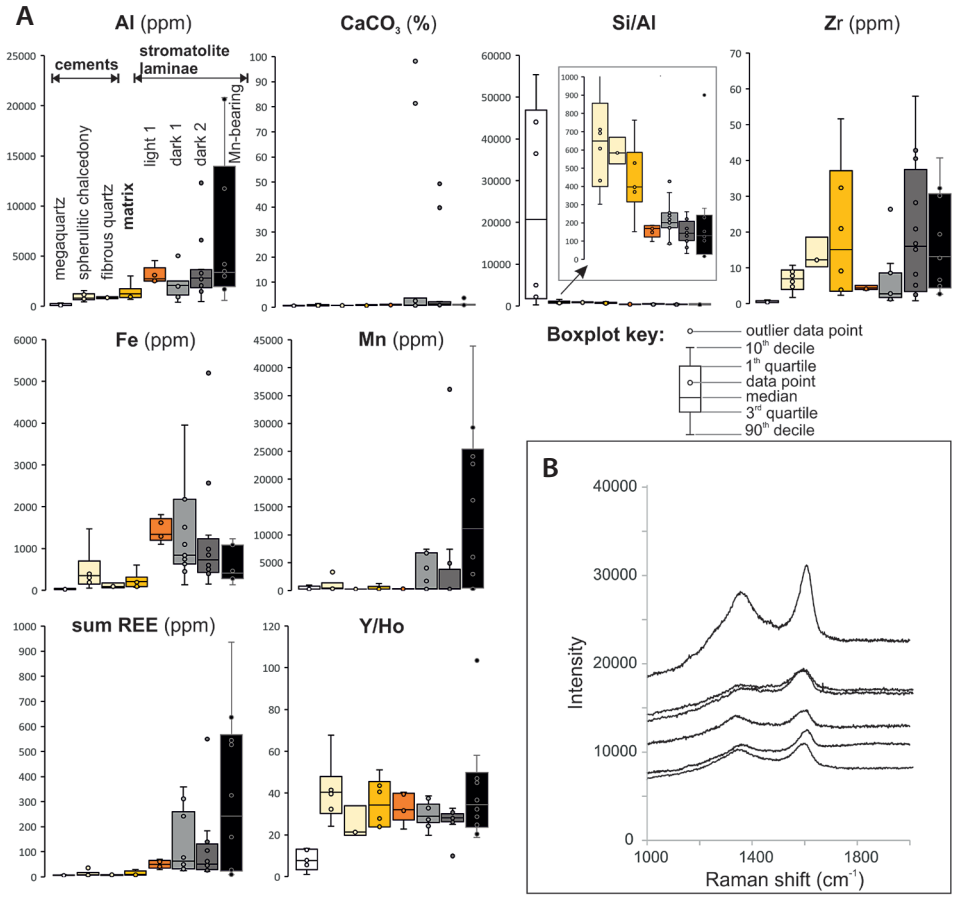

Figure 10. A – boxplot diagrams visualizing variation of concentrations and ratios of selected elements in analysed types of components. Cements were analyzed in the stromatolite type 1 ('finely-crenulate lamination'), light (light 1) and dark (dark 2) stromatolite laminas in type 1 ('finely-crenulate lamination') and dark (dark 2) and Mn-bearing laminas (Mn-bearing) in stromatolite of type 4 ('closely spaced minicolumnar structures'). Matrix was analyzed in samples with both types of stromatolites. B – Raman spectra of thread-like structures of the stromatolite type 1 ('finely-crenulate lamination') and associated openings. Each spectrum depicted was measured from a different part of the structure.

most of the measured spots of stromatolite microstructure type 1 and from some spots of stromatolite microstructure type 4. Of the total number of 60 V/Cr data points, seven reached a value of 2–4.25 indicating hypoxic conditions, and 23 datapoints reached a ratio higher than 4.25, indicating anoxic microenvironments (Jones & Manning 1994). It must be noted that the threshold values used to discriminate redox states in the original study were established based on data from fine-grained siliciclastic rocks. Therefore, interpretations of specific redox conditions derived from V/Cr ratios should be approached with caution and considered merely indicative when applied to silicified stromatolitic carbonates.

Specific geochemical compositions of the particle types (Fig. 10A) indicates that at least parts of the primary and/or early diagenetic elemental composition was preserved during silicification. The question arises as to what proportion of the the original elemental composition was preserved in the siliceous material, as silica crystal lattice has limited potential to incorporate trace and REE elements because of the small size of the Si^{4+} ions (*e.g.* Uysal *et al.* 2011). Most probably, the pseudomorphic replacement of metastable carbonates by SiO_2 phases occurred in the coupled dissolution-precipitation reaction front at the diagenetic fluid-rock interface, and more stable dolomite and Mn- and P-phase inclusions, as well as organic matter, were preserved (Petrash *et al*. 2016) reflecting the primary and very early diagenetic elemental composition.

Raman spectroscopy

Thread-like structures of type 1 ('finely-crenulate lamination') and associated openings were analyzed by Raman spectrometry. The Raman spectrum revealed first-order bands characteristic of organic matter (Fig. 10B), including the D-band at ~ 1350 cm^{-1} and the G-band at 1580 cm^{-1}. (Henry *et al*. 2019). Critically, the documented spectra are distinct from that of the epoxy resin used for thin section preparation, confirming that the analyzed material represents in situ organic matter rather than sample preparation artefacts.

Cathodoluminescence analysis

Cathodoluminescence (CL) analysis revealed distinctly different characteristics between replacement silicification

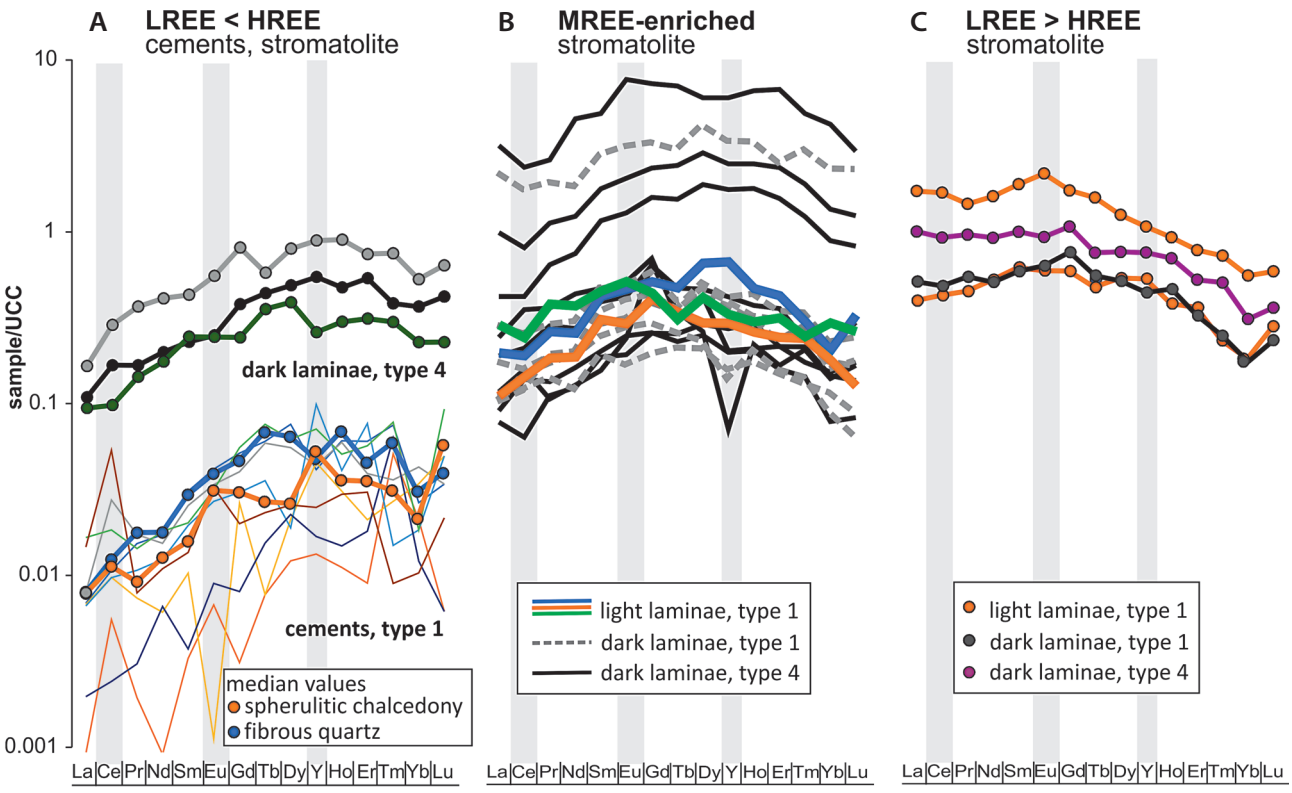

Figure 11. UCC-normalized REE + Y patterns of analyzed stromatolite components. A – LREE-depleted and HREE-enriched pattern of cements of stromatolite type 1 ('finely-crenulate lamination') and dark laminae of stromatolite type 4 ('closely spaced minicolumnar structures'). B – MREE-enriched pattern of light and dark stromatolite laminae of type 1 and 2. C – LREE-enriched/HREE-depleted pattern of stromatolite laminae of type 1 and 4.

and void fillings. While void fillings display distinct growth zonation of subdued/dull purple-brownish CL (Appendix 1.3), the silicified stromatolitic microstructures show two main CL patterns: areas with subtle brownish to reddish colours (Appendix 1.3D), similar in intensity to those observed in void cements, and areas preserving original lamination that exhibit whitish and brown luminescence (Appendix 1.3F). This variable CL response in the silicified stromatolites likely reflects the complex mixture of replacement quartz and remnant dolomitic carbonate with Mn (as confirmed by trace element analysis). Matysová *et al*. (2010) found that even trace amounts of carbonates can significantly affect CL images. While both the stromatolitic microstructures and void fills show similar subdued purple-brownish CL, their distinct quartz textures (microcrystalline in stromatolites *vs*. spherulitic in voids) indicate different silica saturation conditions during formation (Vagle *et al*. 1994, Götze 2012), supporting different timing of these silicification events. As the focus is on the early silicification phase that preserved the stromatolitic microtexture and microstructure, and the mixed mineralogy makes interpretation of the early silicification challenging, CL results will not be discussed further.

Biomarkers and n-alkanes

As mentioned in Material and Methods, the structure represented by finely-crenulate lamination was analyzed for biomarkers, as it represented the most compact, non-porous part (sample 979, Appendix 2). The observed n-alkane distribution (Fig. 12) shows a high amount of n-C_{18} through n-C_{27} homologues with a clear maximum amount of C_{18} and C_{20}, typically associated with aquatic species, such as bacterial and cyanobacterial sources (Eglinton & Hamilton 1963, Derrien *et al*. 2017, Shakeel *et al*. 2015). A markedly low pristane/phytane ratio (Pri/Phy = 0.58) suggests anoxic depositional conditions, which likely represent localized micro-environments within the stromatolitic structure rather than necessarily indicating fully anoxic depositional conditions in the broader environment. Elevated V/Cr ratios and positive Ce and Eu anomalies further support the presence of reducing microenvironmental conditions. The abundant mid-chain alkanes (n-C21 to n-C25) with odd/even predominance value (OEP) of 1,01 might by associated with macrophytes (aquatic higher plants) as observed by Ficken *et al*. (2000) but may also include monomethylalkanes (MMAs) produced by cyanobacteria (Eglinton & Hamilton 1963, Shiea *et al*. 1990, Meyers 2003).

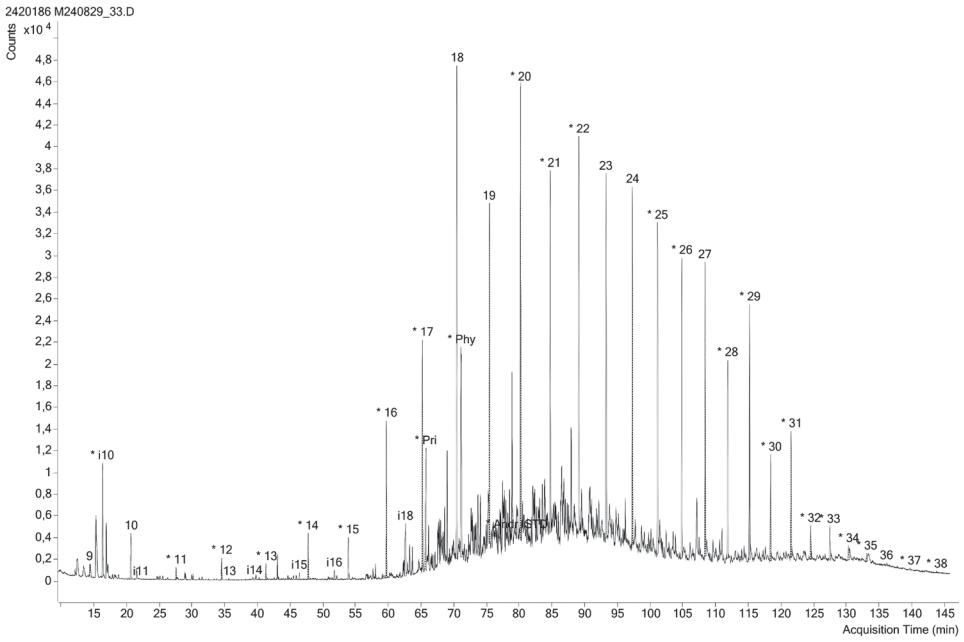

Figure 12. Mass chromatogram (m/z 57) of saturated hydrocarbons of the sample 979 with microstructure type 1, finely-crenulate lamination. The numbers show the number of carbons in n-alkanes, Pri – pristane, and Phy – phytane.

The long-chain n-alkanes (C_{27}–C_{33}) with clearly prevailing odd over even homologues with a carbon preference index (CPI) of 1.4 prove a partial biological source of amorphous organic matter from terrestrial plants. The terrestrial/aquatic plant ratio (TAR; Bourbonniere & Meyers 1996) of 1.33 suggests, that this source is equal to, if not prevailing over the aquatic biota. TAR should be, however, used with caution, because terrestrial plants produce more n-alkanes than algae or cyanobacteria when they live (Peters *et al*. 2005) and hence, TAR of 1 does not mean equal abundance in the source terrestrial and aquatic biota. The abundant hopanoid biomarkers in our sample suggest the presence of a biodegrading prokaryotic community. While hopanoids were traditionally considered indicators of aerobic bacteria (Brocks & Summons 2004), more recent evidence has shown their presence also in sulfate-reducing bacteria, particularly *Desulfovibrio* (Blumenberg *et al*. 2006). This is especially relevant for our laminated stromatolitic material, where vertical zonation of different metabolic groups would be expected (*e.g.* Baumgartner *et al*. 2006). The organic matter in the representative sample had a lower thermal maturity than the oil generation window. The methylphenanthrene index MPI1 (Radke & Welte 1983) corresponds to an equivalent vitrinite reflectance R(MPI1) of 0.49%.

Discussion

Depositional environment

As previously noted, most material was recovered from Quaternary eluvium and colluvium. The stromatolites and oolitic facies were predominantly found as separate silicified boulders, though occurring within a very limited geographic area, suggesting their original spatial proximity. The identical silicification pattern in both stromatolites and oolitic facies further supports their temporal (stratigraphic) relationship. Additionally, two thin sections show direct association of ooids and stromatolites. While these limitations constrain detailed environmental reconstruction, several key observations from individual samples provide insights into local depositional conditions, even if broader paleoenvironmental reconstruction cannot be made.

A vertical association of different stromatolitic microstructures was recorded, comprising: (1) Finely-crenulated lamination, (2) Contiguous, thinly laminated domes, (3) Radial fans, and (4) Closely-spaced minicolumns with gently convex lamination. This vertical association likely reflects fluctuating environmental conditions. The finely-crenulated lamination, characterized by high lamina inheritance, could indicate calmer and more stable environmental conditions. Radial fans are morphologically similar to calcified colonies of modern sheath-forming cyanobacterial taxa, such as *Rivularia* or *Phormidium*. Such colonies, forming fan-like and hemispheroidal shapes with characteristic upright growth, are characteristic for lacustrine, hot spring, and particularly fluvial environments. Their presence may indicate formation under higher energy conditions, possibly under flow regime, as suggested by modern analogues (*e.g.* Pitois *et al*. 2001; Rott *et al*. 2012; Okumura *et al*. 2013a, b; Hägele *et al*. 2006; Tran *et al*. 2019). The polysaccharide sheath covering not only cyanobacterial cells but also entire colonies (Fig. 4B–D, G) could provide

protection against extreme conditions, such as subaerial exposure during periods of low water level.

To sum up, the observed features represented by vertical association of different stromatolitic microstructures and different oolitic facies (*i.e.* facies with poorly sorted, chaotically arranged ooids and oolitic facies with bimodal sorting and longitudinal axes of ooids oriented parallel to bedding) suggest varying water energy conditions and/or water depth. This is compatible with, though not definitively proving, a complex depositional setting such as a lake with periodic stream influence. This would be consistent with previous interpretations of the depositional environment of the Chotěvice Formation as periodic streams and ephemeral playa- to sabkha-type lakes (Prouza & Tásler 2001). However, the interpretation of environmental variability is complicated by several factors. First, pressure solution observed in ooidal samples (Fig. 6A, C) indicates that compaction occurred prior to silicification, suggesting that oolite silicification was significantly later than the early silicification of stromatolites. This temporal difference in diagenetic timing raises the possibility that oolites and stromatolites may represent different stratigraphic intervals. Nevertheless, the co-occurrence of ooids and stromatolite structures in one sample demonstrates that both features existed contemporaneously at some point. Therefore, the observed variability in oolite facies (from chaotically arranged to laminated, bimodally-sorted deposits) could reflect either spatial environmental changes or temporal changes within different stratigraphic levels. Due to the nature of the studied material (eluvium and colluvium) and the inability to observe lateral and vertical relationships between different facies in the field, this environmental interpretation should not be regarded as definitive but rather a hypothesis.

Calcification and preservation of cyanobacterial colonies

Considering the preservation of delicate architecture of forms suggestive of vertical filament orientation (similar to modern *Rivularia*), the encrustation of the microbial microstructures was likely rapid, taking place most probably during the life of the microorganisms (Kempe & Kaźmierczak 1993, Riding 2006). If the calcification took place after the death of the colony, the upright growth mode would not have been preserved. As mentioned above, previous authors interpreted the depositional environment as ephemeral lakes and occasional streams, which is supported by our observations. In such an environment, considering the semi-arid climate, CO_2 degassing driven by evaporation and possibly by water flow likely played a crucial role. This CO_2 withdrawal, further enhanced by photosynthetic activities, would have resulted in increased water alkalinity, creating conditions favourable for carbonate precipitation. Similar rapid encrustation of cyanobacteria is well documented in modern travertines and tufa, where $CaCO_3$ precipitation driven by supersaturation with respect to calcite and CO_2 degassing is considered more significant than precipitation induced by photosynthetic activities (*e.g.* Arp *et al*. 2001, Pentecost 2003, Berrendero *et al*. 2016). The rapid carbonate encrustation of living cyanobacterial colonies not only preserved their growth structures but also created protected microenvironments that enhanced organic matter preservation.

Organic matter preservation and authigenic mineralization

Silica-permineralized organic matter was documented in openings of microstructures (Fig. 7A–H) interpreted as remnants of cyanobacterial cells within calcified and eventually silicified sheaths, as well as within microstructure type 1, 'finely-crenulate lamination', where a C-rich thread associated with aluminosilicates was observed after etching the thin section in 5% HF (Fig. 7I).

It is critical to distinguish between the resin used in thin section preparation, which partly filled pores and cracks, and the syngenetic organic matter. The resin can be differentiated based on distinct shades in BSE images and its location at the rims of the openings (Fig. 7B, C). More importantly, Raman spectroscopy revealed characteristic D and G bands confirming the presence of carbonaceous matter in the openings (Fig. 10B). The biological origin and syngenetic nature of this organic matter is further supported by biomarker composition, which indicates that the maturity of the preserved organic matter corresponds to the geological context. Furthermore, the organic matter exhibits distinctive morphological organization, displaying reticulate patterns that strongly resemble extracellular polymeric substances (EPS) produced by microbial communities (Fig. 7C–E) and filamentous microstructures (Fig. 7F–I). The organic matter consistently occurs in association with characteristic authigenic minerals including iron oxides (and oxidized pyrite), Fig. 7A–C; manganese oxides (Fig. 7H; 8B, C), monazite-group minerals (Fig. 8B, C), aluminosilicates (Fig. 7H, I), and less commonly with minerals of chromite-like composition and Ti oxides (Fig. 7D, H). The association of pyrite (and its diagenetic products) with organic matter is a characteristic result of early diagenetic bacterial sulfate reduction (*e.g.* Berner 1978). The presence of monazite associated with Mn oxides is consistent with high distribution coefficients of Mn oxides for REE, making them effective scavengers

of these elements (*e.g.* Koeppenkastrop & De Carlo 1992). While Mn oxides were sporadically documented in association with organic matter within the openings of microstructure types 1–3, they occur only in low quantities not exceeding 3 wt.%. However, they constitute the main mineral phase (apart from SiO_2) in microstructure type 4. The restricted distribution of these Mn-rich structures to specific microstructure type, their filamentous morphology, and their consistent association with organic matter are compatible with biological influence in their formation, although post-depositional processes have likely modified their original characteristics. The association of aluminosilicates with microbial surfaces is a well-documented phenomenon, where organic surfaces, particularly EPS, provide nucleation sites for clay mineral formation (*e.g*. Konhauser & Urrutia 1999). Similarly, the presence of Ti- and Cr-bearing phases in association with microbial organic matter could be the result of microbially mediated precipitation (*e.g.* Kang *et al*. 2007, Bower *et al*. 2015). The exceptional preservation of organic matter and associated authigenic minerals provides key evidence for the timing of silicification, as such delicate biological microstructures would not have survived without early mineralization.

Silicification pattern and timing of silicification

There are several lines of evidence that the SiO_2 replacement of the carbonate phase in stromatolitic structures was early diagenetic. This early silicification phase consists of micro- to cryptocrystalline quartz that replaced the primary carbonate fabric (Figs 3E; 9A–C, F), while meticulously preserving its original microtextural, micro- and macrostructural characteristics. Areas originally composed of micritic carbonate are now preserved as equant crypto-microcrystalline quartz, whereas zones likely formed by early carbonate cement are replaced by slightly larger quartz microcrystals. The precise preservation of primary textures alone does not prove early silicification, as similar texture-preserving silicification can occur after burial diagenesis (*e.g.* Maliva 2001). However, early diagenetic replacement is further supported by the preservation of primary porosity, the preservation of delicate stromatolitic microstructures (represented by convex geometry), and the preservation of primary/early diagenetic REE and trace elements composition. The most compelling evidence for very early silicification, occurring during earliest diagenesis likely at the lake bottom or within shallow subsurface sediment, is the preservation of organic matter within openings interpreted as remnants of cyanobacterial cells, comprising C-rich masses, filaments, and EPS-like microstructures with authigenic minerals. Without rapid mineralization, such microbial organic matter would decay within days to weeks (Bartley 1996), as illustrated by the absence of silicified organic remains in thin sections of stromatolites with primary carbonate mineralization, where microbial remains were observed only within the openings. Kremer *et al.* (2012) document a similar example of calcified microstructures lacking preserved microbial remains, in contrast to extremely well-preserved microstructures produced by silica mineralization.

To sum up, four main lines of evidence support our interpretation of very early silicification of the stromatolites: (1) silicification of organic matter, (2) preservation of delicate microtexture as well as micro- and macrostructural stromatolite architecture, (3) preservation of primary porosity, and (4) preservation of primary/early diagnetic REE and trace element composition.

Source of silica

Although the character of the samples (mostly eluvial and colluvial deposits) limits our ability to reconstruct the complete depositional system, multiple lines of evidence suggest that volcanoclastic input was the most likely source of silica. Two key features were observed in thin sections of oolitic rocks: (1) grains with brownish rims possessing glassy isotropic groundmass that were found in the matrix as well as in the ooidal cortices and cores (Fig. 6D, E), and (2) well-sorted, minute (2–8 μm) sanidine crystals (high-temperature form of K-feldspar) that occur both in the matrix and aligned along the ooidal cortices laminae (Fig. 6F). These observations indicate syndepositional input of volcanoclastic material, during the formation of ooids. While erosion of volcanic rocks could potentially contribute some volcanic-derived material, the presence of glassy groundmass with only minor brown alteration rims and euhedral minute sanidine crystals aligned within ooidal cortex laminae strongly suggests minimal transport and reworking, pointing to contemporaneous volcanic input. The well-sorted sanidine within the ooidal cortices specifically suggests deposition from volcanic ash fall. The extremely fine grain size of these crystals would allow them to remain in suspension longer than coarser materials, becoming integrated into the cortices during periods of less turbulent conditions. Although oolites and stromatolites were found within eluvial deposits, their restricted geographic distribution suggests close spatial and stratigraphic relationship, supported by the two samples showing association of stromatolites with ooids (Appendix 1.1D, E).

Active rhyolitic and andesitic volcanism during the sedimentation of the Prosečné and Chotěvice formations has been documented in the KPB. During the late Carbon-

iferous-early Permian transition, numerous silica-rich, high-volume volcanic complexes developed in western and central European basins due to the late Variscan postorogenic extensional regime (Awdankiewicz *et al*. 2024). Notably, previous authors documented also cherts associated with tuffitic layers in both the Prosečné and Chotěvice formations (Prouza & Tásler 2001), which further supports the role of volcanic material in silicification.

A question arises whether volcanoclastic material alone could have provided sufficient silica for pervasive stromatolite silicification. Authors, who studied silica permineralized woods from the KPB suggested as most probable source of silica weathering of labile minerals, in particular feldspars due to preferential occurrence of silicified wood in fluvial arkoses and arkosic sands (Purkyně 1927, Skoček 1970, Matysová *et al*. 2010). While dissolution of feldspars in arkoses likely provided silica for wood permineralization in arkose-rich deposits, the stromatolites reported herein formed in different facies, associated with fine-grained silicified rocks containing ooids. Although arkoses occur in certain intervals of the Prosečné Formation, they are not the dominant lithology. As noted by Prouza & Tásler (2001), the Prosečné Formation represents the finest-grained lithology in Carboniferous and Permian deposits in the KPB. The overlying Chotěvice Formation consists of irregularly alternating conglomerates, breccias, sandstones, and mudrocks, with the latter forming up to 100 m thick intervals at the formation's top. While feldspar weathering could represent an important silica source for certain intervals, particularly in arkose-rich facies, we favour the interpretation that volcanoclastic material, for which we have direct evidence of contemporaneous deposition, represents the primary source of silica for the silicification of ooids, stromatolites and associated sediments.

Another potential source of silica could have been hydrothermal fluids, as the active magmatism during the late Carboniferous–early Permian transition likely generated hydrothermal activity in the basin. However, our REE analysis does not support the hydrothermal scenario, nor is there evidence for hydrothermal mineralization in the Mladé Buky vicinity.

In summary, given the association of tuffitic horizons with silicites noted by previous authors and the direct evidence of synsedimentary deposition of volcanoclastic material in our study, particularly the sanidine crystals and glassy components within ooidal cortices, we consider contemporaneous volcanic ash fall as a probable silica source for the early silicification phase of both stromatolites and oolites. However, we cannot completely rule out some contribution from erosion of older volcanic deposits. As pointed out by Krainer & Spötl (1998), silica supersaturation is a common feature in aquatic environments surrounded by acidic volcanic rocks. Regardless of the specific volcanic input mechanism (either volcanic ashfall or erosion of volcanic rocks), this material likely provided the necessary silica for the exceptional preservation observed in the stromatolites.

The critical aspect of silica enrichment concerns the mechanism by which silica-rich fluids were liberated from glassy volcanoclastic material. While the dissolution of silica phases is generally enhanced at pH > 9 (Krauskopf 1956), glassy volcanoclastic material, being metastable, would have been susceptible to dissolution even under slightly less alkaline conditions (White *et al*. 1980). Several lines of evidence suggest that the lake water chemistry was likely alkaline (*e.g.* rapid calcification of microbial structures, positive Ce and Eu anomalies). Under alkaline conditions, Si-rich pyroclastic material would undergo rapid dissolution, generating silica-rich solutions. This dissolution process would eventually lead to localized pH decrease, promoting silica precipitation and subsequent replacement of carbonate of the stromatolites. Keeping in mind the limitations of direct comparisons with modern environments, similar processes can be observed in several modern alkaline volcanic lakes of elevated pH values (pH > 9). These include Lake Specchio di Venere in Italy, which features siliceous stromatolites and carbonate-rich microbial mats (Cangemi *et al*. 2010, Censi *et al*. 2015); Lake Van and Mt. Nemrut Soğuk Lake in Turkey, where both siliceous and carbonate mat development occurs (Budakoglu 2009); and the caldera lake of Niuafo'ou Island in the southern Pacific, where both carbonate and silica mineralization of stromatolites have been documented (Kazmierczak & Kempe 2006, Kremer *et al*. 2012).

Conclusions

Keeping in mind the limitations resulting from the eluvial and colluvial nature of our samples, we present the following key findings and interpretations:

The stromatolites formed in a very shallow, likely alkaline fluvio-lacustrine setting characterized by fluctuating environmental conditions, as suggested by the vertical succession of different stromatolitic forms and various oolitic facies. Characteristic components of the microbial community were sheath-forming cyanobacterial taxa similar to modern *Rivularia*, whose protective sheaths may have enabled survival during potential subaerial exposure.

The exceptional preservation of these structures appears to have resulted from a two-stage process. Initial rapid calcification, suggested by preserved upright growth architecture, likely occurred in alkaline waters where CO_2 withdrawal could have been enhanced by evaporation, water flow, and photosynthetic activity. Subsequently, contemporaneous deposition of metastable volcanoclastic material generated SiO_2-rich solutions. This led to early

diagenetic silicification that both permineralized the remaining organic matter and replaced the $CaCO_3$ encrustations, presumably taking place at or near the depositional interface. The microstructure- and microtexture-retentive nature of this silicification preserved primary features that would typically be lost through carbonate recrystallization.

Biomarker and n-alkane distributions in the analyzed samples indicate that the organic matter originated from a mixed community dominated by cyanobacteria and other aquatic microbes, with a contribution from terrestrial plant-derived organic matter.

While the nature of our samples precludes broader paleoenvironmental reconstructions, these exceptionally well-preserved specimens provide a rare glimpse into early Permian terrestrial environments and their microbial communities. The combination of rapid carbonate precipitation and early silicification created a unique preservation window, protecting not only delicate stromatolitic structures but also organic matter that would typically be lost through diagenesis.

Acknowledgements

This research was funded by the Czech Science Foundation (GAČR, project GC20-20785J). It also represents a contribution to the Strategic Research Plan of the Czech Geological Survey (DKRVO/CGS 2023–2027, 311 740). We would like to thank Karel Martínek (Charles University in Prague) and Steffen Trümper (Museum für Naturkunde Chemnitz, Germany) for their thorough reviews and constructive feedback, which significantly improved the quality of this manuscript. We thank Jiří Komárek for valuable discussions on cyanobacterial morphology. Field work assistance by Radovan Vlček, Josef Konečný, and Zdeněk Venera is gratefully acknowledged. We appreciate constructive discussions on regional geology and volcanism with Jiří Morysek, Roland Nádaskay, Vladislav Rapprich, and Marcela Stárková (Czech Geological Survey, Prague). We are grateful to Jaromír Leichmann for assistance with optical cathodoluminescence analyses and to Radek Škoda for providing a stromatolite sample. While we are thankful for the assistance of numerous colleagues, any errors or misinterpretations are solely the responsibility of the authors. We are thankful to the editorial team of the Bulletin of Geosciences for their professional handling of the manuscript during the review process and the preparation of the final article.

References

Allwood, A., Walter, M., Kamber, B., Marshall, C.P. & Burch, I.W. 2006. Stromatolite reef from the Early Archaean era of Australia. *Nature 441*, 714–718. DOI 10.1038/nature04764

Andrews, S.D. & Trewin, N.H. 2014. Palaeoenvironmental significance of lacustrine stromatolite forms from the Middle Old Red Sandstone of the Orcadian Basin. *Geological Magazine* 151, 414–429. DOI 10.1017/S0016756813000290

Arp, G., Wedemeyer, N. & Reitner, J. 2001. Fluvival tufa formation in a hard-water creek (Deinschwanger Bach, Franconian Alb, Germany). *Facies 44*, 1–22. DOI 10.1007/BF02668163

Awdankiewicz, M., Pańczyk, M., Ploch, I., Raczyński, P., Awdankiewicz, H., Górecka-Nowak, A., Pawlak, W. & Peryt, T. 2024. Timing of post-orogenic silicic volcanism in the eastern part of the European Variscides: constraints from SHRIMP U–Pb zircon study of the Permo-Carboniferous Góry Suche Rhyolitic Tuffs (the Intra-Sudetic Basin). *International Journal of Earth Sciences 113*, 1–21. DOI 10.1007/s00531-024-02474-y

Bai, Y., Liu, Z., Sun, P., Liu, R., Hu, X., Zhao, H. & Xu, Y. 2015. Rare earth and major element geochemistry of Eocene fine-grained sediments in oil shale- and coal-bearing layers of the Meihe Basin, Northeast China. *Journal of Asian Earth Sciences 97*, 89–101. DOI 10.1016/j.jseaes.2014.10.008

Bartley, J.K. 1996. Actualistic taphonomy of cyanobacteria: implications for the Precambrian fossil record. *Palaios 11(6)*, 571–586. DOI 10.2307/3515192

Bartley, J.K., Knoll, A.H., Grotzinger, J.P. & Sergeev, V.N. 2000. Lithification and Fabric Genesis in Precipitated Stromatolites and Associated Peritidal Carbonates, Mesoproterozoic Billyakh Group, Siberia, 59–73. *In* Grotzinger, J.P. & James, N.P. (eds) *Carbonate Sedimentation and Diagenesis in the Evolving Precambrian World*. SEPM Society for Sedimentary Geology, Tulsa. DOI 10.2110/pec.00.67.0059

Bau, M. 1991. Rare earth element mobility during hydrothermal and metamorphic fluid–rock interaction and the significance of the oxidation state of europium. *Chemical Geology 93*, 219–230. DOI 10.1016/0009-2541(91)90115-8

Bau, M., Koschinsky, A., Dulski, P. & Hein, J. 1996. Comparison of the partitioning behaviours of yttrium, rare earth elements, and titanium between hydrogenetic marine ferromanganese crusts and seawater. *Geochimica et Cosmochimica Acta 60*, 1709–1725. DOI 10.1016/0016-7037(96)00063-4

Bau, M., Schmidt, K., Koschinsky, A., Hein, J., Kuhn, T. & Usui, A. 2014. Discriminating between different genetic types of marine ferro-manganese crusts and nodules based on rare earth elements and yttrium. *Chemical Geology 381*, 1–9. DOI 10.1016/j.chemgeo.2014.05.004

Baumgartner, L.K., Reid, R.P., Dupraz, C., Decho, A.W., Buckley, D.H., Spear, J.R., Przekop, K.M. & Visscher, P.T. 2006. Sulfate reducing bacteria in microbial mats: Changing paradigms, new discoveries. *Sedimentary Geology 185*, 131–145. DOI 10.1016/j.sedgeo.2005.12.008

Berner, R.A. 1978. Sulfate reduction and the rate of deposition of marine sediments. *Earth and Planetary Science Letters 37*, 492–498. DOI 10.1016/0012-821X(78)90065-1

Berrendero, E., Arenas, C., Mateo, P. & Jones, B. 2016. Cyanobacterial diversity and related sedimentary facies as a function of water flow conditions: Example from the Mona-

sterio de Piedra Natural Park (Spain). *Sedimentary Geology 337*, 12–28. DOI 10.1016/j.sedgeo.2016.03.003

Bertrand-Sarfati, J. & Fabre, J. 1974. Les stromatolites nodulaires de l'Autunien lacustre du bassin d'Abadla-Bechar (Sahara occidental Algérien). *Bulletin de la Société d'Histoire Naturelle de l'Afrique du Nord 40*, 179–206.

Blakey, R. 2020 *Global Paleogeography and Tectonics in Deep Time Series*. *https://deeptimemaps.com/*

Blecha, M., Martínek, K. & Mihaljevič, M. 1999. Paleoenvironmental changes of the semipermanent Kalna Lake (Lower Permian), Krkonose Piedmont Basin, Czech Republic. *Acta Universitatis Carolinae, Geologica 43(4)*, 657–665.

Blumenberg, M., Krüger, M., Nauhaus, K., Talbot, H.M., Oppermann, B.I., Seifert, R., Pape, T. & Michaelis, W. 2006. Biosynthesis of hopanoids by sulfate-reducing bacteria (genus *Desulfovibrio*). *Environmental Microbiology 8*, 1220–1227. DOI 10.1111/j.1462-2920.2006.01014.x

Bosak, T., Liang, B., Sim, M.S. & Petroff, A.P. 2009. Morphological record of oxygenic photosynthesis in conical stromatolites. *Proceedings of the National Academy of Sciences USA 106*, 10939–10943. DOI 10.1073/pnas.0900885106

Bourbonniere, R.A. & Meyers, P.A. 1996. Sedimentary geolipid records of historical changes in the watersheds and productivities of Lakes Ontario and Erie. *Limnology and Oceanography 41*, 352–359.
DOI 10.4319/lo.1996.41.2.0352

Bower, D.M., Hummer, D.R., Steele, A. & Kyono, A. 2015. The Co-evolution of Fe-oxides, Ti-oxides, and other microbially induced mineral precipitates in sandy sediments: understanding the role of cyanobacteria in weathering and early diagenesis. *Journal of Sedimentary Research 85*, 1213–1227. DOI 10.2110/jsr.2015.76

Brocks, J.J. & Summons, R.E. 2004. Sedimentary hydrocarbons, biomarkers for early life, 61–103. *In* Holland, H.D. & Turekian, K.K. (eds) *Treatise on Geochemistry*, *Second Edition, Vol. 10*. Elsevier, Amsterdam & Boston.
DOI 10.1016/B978-0-08-095975-7.00803-2

Budakoglu, M. 2009. Comparison of Recent Siliceous and Carbonate Mat Development on the Shore of Hyper-Alkaline Lake Van and Mt. Nemrut Soğuk Lake, NE Anatolia, Turkey. *Geomicrobiology Journal 26*, 146–160.
DOI 10.1080/01490450802675027

Burne, R.V. & Moore, L.S. 1987. Microbialites: Organosedimentary Deposits of Benthic Microbial Communities. *Palaios 2(3)*, 241–254. DOI 10.2307/3514674

Campbell, K.A., Lynne, B.Y., Handley, K.M., Jordan, S., Farmer, J.D., Guido, D.M., Foucher, F., Turner, S. & Perry, R.S. 2015. Tracing Biosignature Preservation of Geothermally Silicified Microbial Textures into the Geological Record. *Astrobiology 15*, 858–882.
DOI 10.1089/ast.2015.1307

Cangemi, M., Bellanca, A., Borin, S., Hopkinson, L., Mapelli, F. & Neri, R. 2010. The genesis of actively growing siliceous stromatolites: Evidence from Lake Specchio di Venere, Pantelleria Island, Italy. *Chemical Geology 276*, 318–330. DOI 10.1016/j.chemgeo.2010.06.017

Cao, R. 1991. Origin and order of cyclic growth patterns in matministromatolite bioherms from the Proterozoic Wumishan formation, North China. *Precambrian Research 52*, 167–178. DOI 10.1016/0301-9268(91)90018-6

Casanova, J. & Hillaire-Marcel, C. 1992. Late Holocene hydrological history of Lake Tanganyika, East Africa, from isotopic data on fossil stromatolites. *Palaeogeography, Palaeoclimatology, Palaeoecology 91*, 35–48.
DOI 10.1016/0031-0182(92)90030-9

Cathalot, C., Roussel, E.G., Perhirin, A., Creff, V., Donval, J., Guyader, V. & Sarradin, P. 2021. Hydrothermal plumes as hotspots for deep-ocean heterotrophic microbial biomass production. *Nature Communications 12(1)*, 26877.
DOI 10.1038/s41467-021-26877-6

Caudwell, C., Lang, J. & Pascal, A. 2001. Lamination of swampy-rivulets *Rivularia haematites* stromatolites in a temperate climate. *Sedimentary Geology 143*, 125–147.
DOI 10.1016/S0037-0738(00)00191-3

Censi, P., Cangemi, M., Brusca, L., Madonia, P., Saiano, F. & Zuddas, P. 2015. The behavior of rare-earth elements, Zr and Hf during biologically-mediated deposition of silica-stromatolites and carbonate-rich microbial mats. *Gondwana Research 27*, 209–215. DOI 10.1016/j.gr.2013.09.014

Centeno, C.M., Legendre, P., Beltrán, Y., Alcántara-Hernández, R.J., Lidström, U.E., Ashby, M.N. & Falcón, L.I. 2012. Microbialite genetic diversity and composition relate to environmental variables. FEMS *Microbiology Ecology 82*, 724–735. DOI 10.1111/j.1574-6941.2012.01447.x

Deng, Y., Ren, J., Guo, Q., Cao, J., Wang, H. & Liu, C. 2017. Rare earth element geochemistry characteristics of seawater and porewater from deep sea in western Pacific. *Scientific Reports 7*, 16539.
DOI 10.1038/s41598-017-16379-1

Derrien, M., Yang, L. & Hur, J. 2017. Lipid biomarkers and spectroscopic indices for identifying organic matter sources in aquatic environments: A review. *Water Research 112*, 58–71. DOI 10.1016/j.watres.2017.01.023

Donaldson, J.A. 1976. Paleoecology of Conophyton and Associated Stromatolites in the Precambrian Dismal Lakes and Rae Groups, Canada, 523–534. *In* Walter, M.R. (ed.) *Stromatolites Developments in Sedimentology*. Elsevier, Amsterdam. DOI 10.1016/S0070-4571(08)71156-7

Dragastan, O. & Mišík, M. 2001. Non-marine Lower Cretaceous algae and cyanobacteria from the Czorsztyn Unit, Western Carpathians. *Geologica Carpathica 52(4)*, 229–237.

Dupraz, C., Reid, R.P., Braissant, O., Decho, A.W., Norman, R.S. & Visscher, P.T. 2009. Processes of carbonate precipitation in modern microbial mats. *Earth-Science Reviews 96*, 141–162. DOI 10.1016/j.earscirev.2008.10.005

Eglinton, G. & Hamilton, R.J. 1963. The distribution of alkanes, 187–215. *In* Swain, T. (ed.) *Chemical Plant Taxonomy*. 543 pp. Academic Press, London.
DOI 10.1016/B978-0-12-395540-1.50012-9

Elster, J., Nedbalová, L., Vodrážka, R., Láska, K., Haloda, J. & Komárek, J. 2016. Unusual biogenic calcite structures in two shallow lakes, James Ross Island, Antarctica. *Biogeosciences 13*, 535–549. DOI 10.5194/bg-13-535-2016

Faltusová, V., Vaculovič, T., Holá, M. & Kanický, V. 2022. Ilaps – python software for data reduction and imaging with LA-ICP-MS. *Journal of Analytical Atomic Spectrometry 37*, 733–740. DOI 10.1039/D1JA00383F

Fediuk, F. 1956. Křemitá oolitická hmota v podkrkonošském permokarbonu. *Časopis pro mineralogii a geologii 1–2*, 208–210.

Fernandez-Turiel, J.L., Garcia-Valles, M., Gimeno-Torrente, D., Saavedra-Alonso, J. & Martinez-Manent, S. 2005. The hot spring and geyser sinters of El Tatio, Northern Chile. *Sedimentary Geology 180*, 125–147. DOI 10.1016/j.sedgeo.2005.07.005

Ficken, K.J., Li, B., Swain, D.L., Eglinton, G. 2000. An n-alkane proxy for the sedimentary input of submerged/floating freshwater aquatic macrophytes. *Organic Geochemistry 31*, 745–749.
DOI 10.1016/S0146-6380(00)00081-4

Frantz, C.M., Petryshyn, V.A., Marenco, P.J., Tripati, A., Berelson, W.M. & Corsetti, F.A. 2014. Dramatic local environmental change during the Early Eocene Climatic Optimum detected using high resolution chemical analyses of Green River Formation stromatolites. *Palaeogeography, Palaeoclimatology, Palaeoecology 405*, 1–15. DOI 10.1016/j.palaeo.2014.04.001

Freytet, P. & Plet, A. 1991. Les formations stromatolitiques (tufs calcaires) récentes de la région de Tournus (Saône et Loire). *Geobios 24*, 123–139. DOI 10.1016/S0016-6995(91)80001-G

Freytet, P. & Plet, A. 1996. Modern freshwater microbial carbonates: the Phormidium stromatolites (tufa-travertine) of southeastern Burgundy (Paris Basin, France). *Facies 34*, 219–237. DOI 10.1007/BF02546166

Freytet, P. & Verrecchia, E.P. 1998. Freshwater organisms that build stromatolites: a synopsis of biocrystallization by prokaryotic and eukaryotic algae. *Sedimentology 45*, 535–563. DOI 10.1046/j.1365-3091.1998.00155.x

Freytet, P., Lebreton, M.-L. & Paquette, Y. 1992. The carbonates of the Permian Lakes of North Massif central, France. *Carbonates and Evaporites 7*, 122–131. DOI 10.1007/BF03175626

Freytet, P., Kerp, H. & Broutin, J. 1996. Permian freshwater stromatolites associated with the conifer shoots Cassinisia orobica Kerp et al. – a very peculiar type of fossilization. *Review of Palaeobotany and Palynology 91*, 85–105. DOI 10.1016/0034-6667(95)00078-X

Freytet, P., Toutin-Morin, N., Broutin, J., Debriette, P., Durand, M., El Wartiti, M., Gand, G., Kerp, H., Orszag, F., Paquette, Y., Ronchi, A. & Sarfati, J. 1999. Palaeoecology of non marine algae and stromatolites: Permian of France and adjacent countries. *Annales de Paléontologie 85*, 99–153. DOI 10.1016/S0753-3969(99)80010-X

Gand, G., Stapf, K.R., Broutin, J. & Debriette, P. 1993. The importance of silicified wood, stromatolites for the paleoecology and the stratigraphy in the Lower Permian of the northeastern Blanzy–Le Creusot Basin (Massif Central, France). *Newsletters on Stratigraphy 28*, 1–32. DOI 10.1127/nos/28/1993/1

Gao, P., He, Z., Lash, G.G., Li, S., Xiao, X., Han, Y. & Zhang, R. 2020. Mixed seawater and hydrothermal sources of nodular chert in Middle Permian limestone on the eastern Paleo-Tethys margin (South China). *Palaeogeography, Palaeoclimatology, Palaeoecology 551*, 109740. DOI 10.1016/j.palaeo.2020.109740

Garnit, H., Bouhlel, S., Barca, D. & Chtara, C. 2012. Application of LA-ICP-MS to sedimentary phosphatic particles from Tunisian phosphorite deposits: Insights from trace elements and REE into paleo-depositional environments. *Geochemistry 72(2)*, 127–139. DOI 10.1016/j.chemer.2012.02.001

Glunk, C., Dupraz, C., Braissant, O., Gallagher, K.L., Verrecchia, E.P. & Visscher, P.T. 2011. Microbially mediated carbonate precipitation in a hypersaline lake, Big Pond (Eleuthera, Bahamas). *Sedimentology 57(7)*, 1801–1819.

Golubić, S., Violante, C., Plenković-Moraj, A. & Grgasović, T. 2008. Travertines and calcareous tufa deposits: an insight into diagenesis. *Geologia Croatica 61(2)*, 363–378. DOI 10.4154/gc.2008.28

Götze, J. 2012. Application of cathodoluminescence microscopy and spectroscopy in geosciences. *Microscopy and microanalysis 18(6)*, 1270–1284. DOI 10.1017/S1431927612001122

Grey, K. & Awramik, S.M. 2020. Handbook for the study and description of microbialites. *Geological Survey of Western Australia, Bulletin 147*, 1–278.

Guido, D.M., Campbell, K.A., Foucher, F. & Westall, F. 2019. Life is everywhere in sinters: examples from Jurassic hot-spring environments of Argentine Patagonia. *Geological Magazine 156*, 1631–1638. DOI 10.1017/S0016756819000815

Hägele, D., Leinfelder, R., Grau, J., Burmeister, E.-G. & Struck, U. 2006. Oncoids from the river Alz (southern Germany): Tiny ecosystems in a phosphorus-limited environment. *Palaeogeography, Palaeoclimatology, Palaeoecology 237*, 378–395. DOI 10.1016/j.palaeo.2005.12.016

Haley, B.A., Klinkhammer, G.P. & McManus, J. 2004. Rare earth elements in pore waters of marine sediments. *Geochimica et Cosmochimica Acta 68*, 1265–1279. DOI 10.1016/j.gca.2003.09.012

Hellwig, A., Trümper, S., Rössler, R. & Krings, M. 2023. Freshwater stromatolites from an Early Permian wetland (Manebach, Thuringian-Forest Basin, Germany): Structure, development, and paleoenvironmental context. *Palaios 38(9)*, 353–370. DOI 10.2110/palo.2022.049

Henry, D.G., Jarvis, I., Gillmore, G. & Stephenson, M. 2019. Raman spectroscopy as a tool to determine the thermal maturity of organic matter: Application to sedimentary, metamorphic and structural geology. *Earth Science Reviews 198*, 102936. DOI 10.1016/j.earscirev.2019.102936

Hmich, D., Schneider, J.W., Saber, H., Voigt, S. & El Wartiti, M. 2006. New continental Carboniferous and Permian faunas of Morocco: implications for biostratigraphy, palaeobiogeography and palaeoclimate, 297–324. *In* Lucas, S.G., Cassinis, G. & Schneider, J.W. (eds) *Non-Marine Permian*

Biostratigraphy and Biochronology. *Geological Society London, Special Publication 265*.
DOI 10.1144/GSL.SP.2006.265.01.14

Hofmann, H.J. 1969. Attributes of stromatolites. *Geological Survey of Canada Paper 69(39)*, 1–58. DOI 10.4095/106437

Hofmann, H.J. & Jackson, G.D. 1987. Proterozoic ministromatolites with radial-fibrous fabric. *Sedimentology 34*, 963–971. DOI 10.1111/j.1365-3091.1987.tb00586.x

Holland, S.M. 2016. The non-uniformity of fossil preservation. *Philosophical Transactions of the Royal Society B 371*, 20150130. DOI 10.1098/rstb.2015.0130

Howe, M.A. 1932. The geologic importance of the lime-secreting algae, with a description of a new travertine-forming organism. *Professional Paper E*, 57–65. DOI 10.3133/pp170E

Janssen, N., Swennen, R., Podoor, N. & Keppens, E. 1999. Biological and diagenetic influence in Recent and fossil tufa deposits from Belgium. *Sedimentary Geology 126*, 75–95. DOI 10.1016/S0037-0738(99)00033-0

Jiang, L., Cai, C., Worden, R.H., Li, K., Xiang, L., Chu, X., Shen, A. & Li, W. 2015. Rare earth element and yttrium (REY) geochemistry in carbonate reservoirs during deep burial diagenesis: Implications for REY mobility during thermochemical sulfate reduction. *Chemical Geology 415*, 87–101. DOI 10.1016/j.chemgeo.2015.09.010

Jones, B. & Manning, D.A.C. 1994. Comparison of geochemical indices used for the interpretation of palaeoredox conditions in ancient mudstones. *Chemical Geology 111*, 111–129.
DOI 10.1016/0009-2541(94)90085-X

Jones, B., Renaut, R.W. & Konhauser, K.O. 2005. Genesis of large siliceous stromatolites at Frying Pan Lake, Waimangu geothermal field, North Island, New Zealand. *Sedimentology 52(6)*, 1229–1252. DOI 10.1111/j.1365-3091.2005.00739.x

Kah, L.C. & Knoll, A.H. 1996. Microbenthic distribution of Proterozoic tidal flats: Environmental and taphonomic considerations. *Geology 24*, 79–82.
DOI 10.1130/0091-7613(1996)024<0079:MDOPTF>2.3.CO;2

Kang, S.-Y., Lee, J.-U. & Kim, K.-W. 2007. Biosorption of Cr(III) and Cr(VI) onto the cell surface of *Pseudomonas aeruginosa*. *Biochemical Engineering Journal 36*, 54–58. DOI 10.1016/j.bej.2006.06.005

Kazmierczak, J. & Kempe, S. 2006. Genuine modern analogues of Precambrian stromatolites from caldera lakes of Niuafo'ou Island, Tonga. *Naturwissenschaften 93*, 119–126.
DOI 10.1007/s00114-005-0066-x

Kempe, S. & Kaźmierczak, J. 1993. Satonda Crater Lake, Indonesia: Hydrogeochemistry and biocarbonates. *Facies 28*, 1–31. DOI 10.1007/BF02539726

Kerp, H., Penati, F., Brambilla, G., Clement-Westerhof, J.A. & Van Bergen, P.F. 1996. Aspects of Permian palaeobotany and palynology. XVI. Three-dimensionally preserved stromatolite-incrusted conifers from the Permian of the western Orobic Alps (northern Italy). *Review of Palaeobotany and Palynology 91*, 63–84.
DOI 10.1016/0034-6667(95)00065-8

Kleinteich, J., Golubic, S., Pessi, I.S., Velázquez, D., Storme, J.-Y., Darchambeau, F., Borges, A.V., Compère, P., Radtke, G., Lee, S.-J., Javaux, E.J. & Wilmotte, A. 2017. Cyanobacterial Contribution to Travertine Deposition in the Hoyoux River System, Belgium. *Microbial Ecology 74*, 33–53. DOI 10.1007/s00248-017-0937-7

Koeppenkastrop, D. & De Carlo, E.H. 1992. Sorption of Rare-Earth Elements from Seawater onto Synthetic Mineral Particles—An Experimental Approach. *Chemical Geology 95*, 251–263. DOI 10.1016/0009-2541(92)90015-W

Konhauser, K.O. & Urrutia, M.M. 1999. Bacterial clay authigenesis: a common biogeochemical process. *Chemical Geology 161(4)*, 399–413.
DOI 10.1016/S0009-2541(99)00118-7

Krainer, K. & Spötl, C. 1998. Abiogenic silica layers within a fluvio-lacustrine succession, Bolzano Volcanic Complex, northern Italy: a Permian analogue for Magadi-type cherts? *Sedimentology 45(3)*, 489–505.
DOI 10.1046/j.1365-3091.1998.00164.x

Krauskopf, K.B. 1956. Dissolution and precipitation of silica at low temperatures. *Geochimica et Cosmochimica Acta 10(1–2)*, 1–26. DOI 10.1016/0016-7037(56)90009-6

Kremer, B., Kazmierczak, J., Łukomska-Kowalczyk, M. & Kempe, S. 2012. Calcification and Silicification: Fossilization Potential of Cyanobacteria from Stromatolites of Niuafo'ou's Caldera Lakes (Tonga) and Implications for the Early Fossil Record. *Astrobiology 12*, 535–548.
DOI 10.1089/ast.2011.0742

Lawrence, M.G., Greig, A., Collerson, K.D. & Kamber, B.S. 2006. Rare earth element and yttrium variability in South East Queensland waterways. *Aquatic Geochemistry 12*, 39–72. DOI 10.1007/s10498-005-4471-8

Lucas, S.G., Schneider, J.W. & Cassinis, G. 2006. Non-marine Permian biostratigraphy and biochronology: an introduction. *Geological Society London Special Publications 265*, 1–14. DOI 10.1144/GSL.SP.2006.265.01.01

Maliva, R.G. 2001. Silicification in the Belt Supergroup (Mesoproterozoic), Glacier National Park, Montana, USA. *Sedimentology 48*, 887–896.
DOI 10.1046/j.1365-3091.2001.00399.x

Manning-Berg, A.R. & Kah, L.C. 2017. Proterozoic microbial mats and their constraints on environments of silicification. *Geobiology 15(4)*, 469–483. DOI 10.1111/gbi.12238

Marriott, S.B., Hillier, R.D. & Morrissey, L.B. 2013. Enigmatic sedimentary structures in the Lower Old Red Sandstone, south Wales, UK: possible microbial influence on surface processes and early terrestrial food webs. *Sedimentary Geology 150*, 396–411.
DOI 10.1017/S0016756812000507

Martínek, K., Blecha, M., Daněk, V., Franců, J., Hladíková, J., Johnová, R. & Uličný, D. 2006. Record of palaeoenvironmental changes in a Lower Permian organic-rich lacustrine succession: Integrated sedimentological and geochemical study of the Rudník member, Krkonoše Piedmont Basin, Czech Republic. *Palaeogeography, Palaeoclimatology, Palaeoecology 230*, 85–128.
DOI 10.1016/j.palaeo.2005.07.009

Matysová, P., Rössler, R., Götze, J., Leichmann, J., Forbes, G., Taylor, E.L., Sakala, J. & Grygar, T. 2010. Alluvial and volcanic pathways to silicified plant stems (Upper Carbon-

iferous–Triassic) and their taphonomic and palaeoenvironmental meaning. *Palaeogeography, Palaeoclimatology, Palaeoecology 292*, 127–143. DOI 10.1016/j.palaeo.2010.03.036

McCann, T., Pascal, C., Timmerman, M.J., Krzywiec, P., López-Gómez, J., Wetzel, L., Krawczyk, C.M., Rieke, H. & Lamarche, J. 2006. Post-Variscan (end Carboniferous-Early Permian) basin evolution in Western and Central Europe. *Memoirs of the Geological Society 32*, 355–388. DOI 10.1144/GSL.MEM.2006.032.01.22

McLennan, S.M., 2001. Relationships between the trace element composition of sedimentary rocks and upper continental crust. *Geochemistry, Geophysics, Geosystems 2*, 2000GC000109. DOI 10.1029/2000GC000109

Meyers, P.A. 2003. Applications of organic geochemistry to paleolimnological reconstructions: a summary of examples from the Laurentian Great Lakes. *Organic Geochemistry 34*, 261–289. DOI 10.1016/S0146-6380(02)00168-7

Monty, C.L.V. 1976. The Origin and Development of Cryptalgal Fabrics, 193–249. *In* Walter, M.R. (ed.) *Developments in Sedimentology 20*. Elsevier, Amsterdam. DOI 10.1016/S0070-4571(08)71137-3

Monty, C.L. & Mas, J.R. 1981. Lower Cretaceous (Wealdian) Blue-Green Algal Deposits of the Province of Valencia, Eastern Spain, 85–120. *In* Monty, C. (ed.) *Phanerozoic Stromatolites*. Springer, Berlin. DOI 10.1007/978-3-642-67913-1_9

Munoz-Saez, C., Saltiel, S., Manga, M., Nguyen, C. & Gonnermann, H. 2016. Physical and hydraulic properties of modern sinter deposits: El Tatio, Atacama. *Journal of Volcanology and Geothermal Research 325*, 156–168. DOI 10.1016/j.jvolgeores.2016.06.026

Murphy, R.J., Van Kranendonk, M.J., Baumgartner, R. & Ryan, C. 2021. Biogenicity of Spicular Geyserite from Te Kopia, New Zealand: Integrated Petrography, High-Resolution Hyperspectral and Elemental Analysis. *Astrobiology 21*, 115–135. DOI 10.1089/ast.2019.2067

Myshrall, K.L., Dupraz, C. & Visscher, P.T. 2014. Patterns in Microbialites Throughout Geologic Time: Is the Present Really the Key to the Past? 111–142. *In* Hembree, D.I., Platt, B.F. & Smith, J.J. (eds) *Experimental Approaches to Understanding Fossil Organisms*. Springer, Dordrecht. DOI 10.1007/978-94-017-8721-5_6

Na, L., Li, Q., Krause, C., Zhu, M. & Kiessling, W. 2023. Revisiting the Phanerozoic rock–diversity relationship. *Geological Magazine 160*, 1853–1862. DOI 10.1017/S0016756823000742

Nutman, A., Bennett, V. & Friend, C. 2016. Rapid emergence of life shown by discovery of 3,700-million-year-old microbial structures. *Nature 537*, 535–538. DOI 10.1038/nature19355

Okumura, T., Takashima, C. & Kano, A. 2013a. Textures and processes of laminated travertines formed by unicellular cyanobacteria in Myoken hot spring, southwestern Japan. *Island Arc 22*, 410–426. DOI 10.1111/iar.12034

Okumura, T., Takashima, C., Shiraishi, F., Nishida, S. & Kano, A. 2013b. Processes Forming Daily Lamination in a Microbe-Rich Travertine Under Low Flow Condition at the Nagano-yu Hot Spring, Southwestern Japan. *Geomicrobiology Journal 30(10)*, 910–927. DOI 10.1080/01490451.2013.791355

Opluštil, S., Schmitz, M., Kachlík, V. & Štamberg, S. 2016. Re-assessment of lithostratigraphy, biostratigraphy, and volcanic activity of the Late Paleozoic Intra-Sudetic, Krkonoše-Piedmont and Mnichovo Hradiště basins (Czech Republic) based on new U-Pb CA-ID-TIMS ages. *Bulletin of Geosciences 91*, 399–432. DOI 10.3140/bull.geosci.1603

Opluštil, S., Šimůnek, Z., Zajíc, J. & Mencl, V. 2013. Climatic and biotic changes around the Carboniferous/Permian boundary recorded in the continental basins of the Czech Republic. *International Journal of Coal Geology 119, 114–151*. DOI 10.1016/j.coal.2013.07.014

Paul, S.A., Volz, J.B., Bau, M., Köster, M., Kasten, S. & Koschinsky, A. 2019. Calcium phosphate control of REY patterns of siliceous-ooze-rich deep-sea sediments from the central equatorial Pacific. *Geochimica et Cosmochimica Acta 251*, 56–72. DOI 10.1016/j.gca.2019.02.019

Pentecost, A. 1995. Significance of the biomineralizing micro-niche in a lyngbya (cyanobacterium) travertine. *Geomicrobiology Journal 13*, 213–222. DOI 10.1080/01490459509378022

Pentecost, A. 2003. Taxonomic identity, ecology and distribution of the calcite-depositing cyanobacterium *Phormidium incrustatum* (Oscillatoriaceae). Cryptogamie, *Algologie 24(4)*, 307–321.

Perri, E., Manzo, E. & Tucker, M.E. 2012. Multi-scale study of the role of the biofilm in the formation of minerals and fabrics in calcareous tufa. *Sedimentary Geology 263–264*, 16–29. DOI 10.1016/j.sedgeo.2011.10.003

Peters, K.E., Walters, C.C. & Moldowan, J.M. 2005. *The Biomarker Guide, Volume 2: Biomarkers and Isotopes in Petroleum Systems and Earth History*, *Second Edition*. 471 pp. Cambridge University Press, Cambridge.

Peters, S.E. & Husson, J.M. 2017. Sediment cycling on continental and oceanic crust. *Geology 45*, 323–326. DOI 10.1130/G38861.1

Petrascheck, W.E.W. 1906. Die Schichtfolge im Perm bei Trautenau. *Verhandlungen der Geologischen Bundesanstalt 1906*, 377–383.

Petrash, D.A., Robbins, L.J., Shapiro, R.S., Mojzsis, S.J. & Konhauser, K.O. 2016. Chemical and textural overprinting of ancient stromatolites: Timing, processes, and implications for their use as paleoenvironmental proxies. *Precambrian Research 278*, 145–160. DOI 10.1016/j.precamres.2016.03.010

Pi, D.-H., Liu, C.-Q., Shields, G.A. & Jiang, S.-Y. 2013. Trace and rare earth element geochemistry of black shale and kerogen in the early Cambrian Niutitang Formation in Guizhou province, South China: constraints for redox environments and origin of metal enrichments. *Precambrian Research 225*, 218–229. DOI 10.1016/j.precamres.2011.07.004

Pitois, F., Jigorel, A. & Bertru, G. 2001. Colonization Dynamics of an Encrusting Cyanobacterial Mat in a Hardwater River (Eaulne, France). *Geomicrobiology Journal 18*, 139–155. DOI 10.1080/01490450151143435

Prouza, V. & Tásler, R. 2001. Podkrkonošská pánev, 128–166. *In* Pešek, J. (ed.) *Geologie a ložiska svrchnopaleozoických*

limnických pánví České republiky. Czech Geological Survey, Prague.

Prouza, V., Skoček, V. & Tásler, R. 1977. Evaporites in the Lower Permian of the Krkonoše-piedmont Basin. *Věstník Ústředního ústavu geologického 52*, 367–369.

Purkyně, C. 1927. O nalezištích zkřemenělých kmenů araukaritových v Čechách, zvláště v Podkrkonoší. *Časopis Národního muzea 101*, 113–131.

Radke, M. & Welte, D. 1983. The Methylphenanthrene Index (MPI): A maturity parameter based on aromatic hydrocarbons. *Advances in Organic Geochemistry 1983*, 504–512.

Reid, R.P., Suosaari, E.P., Oehlert, A.M., Pollier, C.G.L. & Dupraz, C. 2024. Microbialite Accretion and Growth: Lessons from Shark Bay and the Bahamas. *Annual Review of Marine Science 16*, 487–511. DOI 10.1146/annurev-marine-021423-124637

Riding, R. 1991. Classification of microbial carbonates, 77–90. In Riding, R. (ed.) *Calcareous Algae and Stromatolites*. Springer, Berlin. DOI 10.1007/978-3-642-52335-9

Riding, R. 2006. Cyanobacterial calcification, carbon dioxide concentrating mechanisms, and Proterozoic–Cambrian changes in atmospheric composition. *Geobiology 4*, 299–316. DOI 10.1111/j.1472-4669.2006.00087.x

Robins, C.R., Deurlington, A., Buck, B.J. & Brock-Hon, A.L. 2015. Micromorphology and formation of pedogenic ooids in calcic soils and petrocalcic horizons. *Geoderma 251–252*, 10–23. DOI 10.1016/j.geoderma.2015.03.009

Roscher, M. & Schneider, J.W. 2006. Permo-Carboniferous climate: Early Pennsylvanian to Late Permian climate development of central Europe in a regional and global context. *Geological Society London, Special Publication 265*, 95–136. DOI 10.1144/GSL.SP.2006.265.01.05

Rössler, R. 2006. Two remarkable Permian petrified forests: correlation, comparison and significance. *Geological Society London, Special Publication 265*, 39–63. DOI 10.1144/GSL.SP.2006.265.01.03

Rössler, R., Trümper, S., Noll, R., Hellwig, A. & Niemirowska, S. 2021. Wood shrinkage during fossilisation and its significance for studying deep-time lignophytes. *Review of Palaeobotany and Palynology 292*, 104455. DOI 10.1016/j.revpalbo.2021.104455

Rott, E., Hotzy, R., Cantonati, M. & Sanders, D. 2012. Calcification types of Oocardium stratum Nägeli and microhabitat conditions in springs of the Alps. *Freshwater Science 31*, 610–624. DOI 10.1899/11.084.1

Saint Martin, J. & Saint Martin, S. 2015. Discovery of calcareous microbialites in coastal ponds of western Sardinia (Italy). *Geo-Eco-Marina 21*, 35–53.

Schäfer, A. & Stapf, K.R.G. 1978. Permian Saar-Nahe Basin and Recent Lake Constance (Germany): Two Environments of Lacustrine Algal Carbonates, 83–107. *In* Matter, A. & Tucker, M.E. (eds) *Modern and Ancient Lake Sediments*. Wiley, Chichester. DOI 10.1002/9781444303698.ch5

Schneider, J. & Romer, R.L. 2010. The Late Variscan Molasses (Late Carboniferous to Late Permian) of the Saxo-Thuringian Zone, 323–346. *In* Linnemann, U. & Romer, R.L. (eds) *Pre-Mesozoic Geology of Saxo-Thuringia - From the Cadomian Active Margin to the Variscan Orogen*. Schweizerbart, Stuttgart.

Schöpfer, K., Nádaskay, R. & Martínek, K. 2022. Evaluation of Climatic and Tectonic Imprints In Fluvial Successions of An Early Permian Depositional System (Asselian Vrchlabí Formation, Krkonoše Piedmont Basin, Czech Republic). *Journal of Sedimentary Research 92*, 275–303. DOI 10.2110/jsr.2020.137

Schovánek, P., Prouza, V., Spudil, J., Dvořák, I., Pecina, V., Skácelová, Z., Tasáryová, Z., Čech, S. & Žáčková, E. 2012. *Základní geologická mapa České republiky 1:25 000, list 03-424 Trutnov*. Česká geologická služba, Praha.

Shakeel, T., Fatma, Z., Fatma, T. & Yazdani, S.S. 2015. Heterogeneity of Alkane Chain Length in Freshwater and Marine Cyanobacteria. *Frontiers in Bioengineering and Biotechnology 3*, 128919. DOI 10.3389/fbioe.2015.00034

Shiea, J., Brassell, S.C. & Ward, D.M. 1990. Mid-chain branched mono- and dimethyl alkanes in hot spring cyanobacterial mats: a direct biogenic source for branched alkanes in ancient sediments? *Organic geochemistry 15*, 223–231. DOI 10.1016/0146-6380(90)90001-G

Shields, G. & Stille, P. 2001. Diagenetic constraints on the use of cerium anomalies as palaeoseawater redox proxies: An isotopic and REE study of Cambrian phosphorites. *Chemical Geology 175*, 29–48. DOI 10.1016/S0009-2541(00)00362-4

Skoček, V. 1970. Silicifikovaná dřeva ve středočeském permokarbonu. *Věstník Ústředního ústavu geologického 45*, 87–94.

Smith, A., Uken, R. & Thackeray, Z. 2005. Cape Morgan peritidal stromatolites: The origin of lamination. *South African Journal of Science 101(3)*, 107–108.

Souza-Egipsy, V., Wierzchos, J., Ascaso, C. & Nealson, K.H. 2005. Mg–silica precipitation in fossilization mechanisms of sand tufa endolithic microbial community, Mono Lake (California). *Chemical Geology 217*, 77–87. DOI 10.1016/j.chemgeo.2004.12.004

Stapf, K.R.G. 1973. Limnische Stromatolithen aus dem pfälzischen Rotliegenden. *Mitteilungen der Pollichia 20*, 103–112.

Stapf, K.R.G. 2005. Stromatolithe und andere Mikrobialithe sowie Kalkalgen im Rotliegend (Permo-Silesium) des Saar-Nahe-Beckens (SW-Deutschland). *Mitteilungen der Pollichia 91*, 21–40.

Stárková, M. & Čáp, P. 2017. Spodněpermské jezerní vápence západní části podkrkonošské pánve, Tatobity (rotliegend). *Zprávy o geologických výzkumech 50*, 35–39.

Suchý, V., Borecká, L., Pachnerová Brabcová, K., Havelcová, M., Svetlik, I., Machovič, V., Lapčák, L. & Ovšonková, Z.A. 2021. Microbial signatures from speleothems: A petrographic and scanning electron microscopy study of coralloids from the Koněprusy Caves (the Bohemian Karst, Czech Republic). *Sedimentology 68(3)*, 1198–1226. DOI 10.1111/sed.12826

Szulc, J. & Cwizewicz, M. 1989. The lower Permian freshwater carbonates of the Slawkow graben, Southern Poland: sedimentary facies context and stable isotope study. *Palaeogeography, Palaeoclimatology, Palaeoecology 70*, 107–120. DOI 10.1016/0031-0182(89)90083-7

Tran, H., Rott, E. & Sanders, D. 2019. Exploring the niche of a highly effective biocalcifier: calcification of the eukaryotic microalga *Oocardium stratum* Nägeli 1849 in a spring stream of the Eastern Alps. *Facies 65*, 37. DOI 10.1007/s10347-019-0578-z

Trümper, S., Vogel, B., Germann, S., Werneburg, R., Schneider, J.W., Hellwig, A., Linnemann, U., Hofmann, M. & Rössler, R. 2023. Decoding the drivers of deep-time wetland biodiversity: insights from an early Permian tropical lake ecosystem. *Palaeontology 66(3)*, e12652. DOI 10.1111/pala.12652

Ulrych, J., Štěpánková, J., Novák, J.K., Pivec, E. & Prouza, V. 2003. Volcanic activity in Late Variscan Krkonose Piedmont Basin: petrological and geochemical constraints. *Slovak Geological Magazine 8(3–4)*, 219–234.

Ulrych, J., Pešek, J., Štepánková-Svobodová, J., Bosák, P., Lloyd, F.E., Seckendorff, V. von, Lang, M. & Novák, J.K. 2006. Permo-Carboniferous volcanism in late Variscan continental basins of the Bohemian Massif (Czech Republic): geochemical characteristic. *Geochemistry 66*, 37–56. DOI 10.1016/j.chemer.2004.02.001

Uysal, T., Gasparon, M., Bolhar, R., Zhao, J-X., Feng, Y.-X. & Jones, G. 2011. Trace element composition of near-surface silica deposits—A powerful tool for detecting hydrothermal mineral and energy resources. *Chemical Geology 280(1–2)*, 154–169. DOI 10.1016/j.chemgeo.2010.11.005

Vagle, G.B., Hurst, A. & Dypvik, H. 1994. Origin of quartz cements in some sandstones from the Jurassic of the Inner Moray Firth (UK). *Sedimentology 41(2)*, 363–377. DOI 10.1111/j.1365-3091.1994.tb01411.x

Walter, M.R., Mcloughlin, S., Drinnan, A.N. & Farmer, J.D. 1998. Palaeontology of Devonian thermal spring deposits, Drummond Basin, Australia. *Alcheringa 22*, 285–314. DOI 10.1080/03115519808619328

White, A.F., Claassen, H.C. & Benson, L. 1980. The effect of dissolution of volcanic glass on the water chemistry in a tuffaceous aquifer, Rainier Mesa, Nevada. *U.S. Geological Survey Water-Supply Paper 1535-Q*, q1–q34.

White, R.A. III, Power, I.M., Dipple, G.M., Southam, G. & Suttle, C.A. 2015. Metagenomic analysis reveals that modern microbialites and polar microbial mats have similar taxonomic and functional potential. *Frontiers in Microbiology 6*, 966. DOI 10.3389/fmicb.2015.00966

Willmer, B.J. & Rasser, M.W. 2022. Calcification patterns of Rivularia-type cyanobacteria: examples from the Miocene of the North Alpine Foreland Basin. *Facies 68*, 16. DOI 10.1007/s10347-022-00654-3

Yang, J., Torres, M., McManus, J., Algeo, T.J., Hakala, J.A. & Verba, C. 2017. Controls on rare earth element distributions in ancient organic-rich sedimentary sequences: role of post-depositional diagenesis of phosphorus phases. *Chemical Geology 466*, 533–544. DOI 10.1016/j.chemgeo.2017.07.003

Zeyen, N., Benzerara, K., Beyssac, O., Daval, D., Muller, E., Thomazo, C., Tavera, R., López-García, P., Moreira, D. & Duprat, E. 2021. Integrative analysis of the mineralogical and chemical composition of modern microbialites from ten Mexican lakes: What do we learn about their formation? *Geochimica et Cosmochimica Acta 305*, 148–184. DOI 10.1016/j.gca.2021.04.030

Supplementary Electronic Material

Appendix 1. Supplementary Data and Figures
Appendix 2. Geochemical data